


RESEARCH ARTICLE | JANUARY 25 2022

Wall shear stress and wall heat flux in a supersonic turbulent boundary layer ^{EP}

Fulin Tong (童福林); Siwei Dong (董思卫) ; Jiang Lai (赖江); ... et. al



Physics of Fluids 34, 015127 (2022)

<https://doi.org/10.1063/5.0079230>



View
Online



Export
Citation

CrossMark

Articles You May Be Interested In

Effect of expansion on the wall heat flux in a supersonic turbulent boundary layer

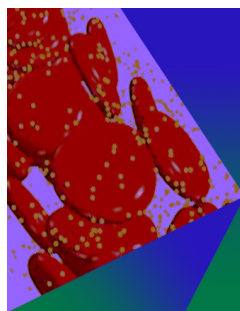
Physics of Fluids (October 2022)

Wall heat flux in a supersonic shock wave/turbulent boundary layer interaction

Physics of Fluids (June 2022)

Enhancement of flame retardancy and mechanical properties of poly(butylene succinate) composites by adding hybrid fillers

AIP Conference Proceedings (October 2020)



Physics of Fluids

Special Topic: Flow and Forensics

Submit Today!

 AIP
Publishing

 AIP
Publishing

Wall shear stress and wall heat flux in a supersonic turbulent boundary layer

Cite as: Phys. Fluids **34**, 015127 (2022); doi: [10.1063/5.0079230](https://doi.org/10.1063/5.0079230)

Submitted: 18 November 2021 · Accepted: 6 January 2022 ·

Published Online: 25 January 2022



View Online



Export Citation



CrossMark

Fulin Tong (童福林),^{1,2}  Siwei Dong (董思卫),^{1,2,a)}  Jiang Lai (赖江),^{1,2} Xianxu Yuan (袁先旭),^{1,2} 
and Xinliang Li (李新亮)^{3,4} 

AFFILIATIONS

¹State Key Laboratory of Aerodynamics, China Aerodynamics Research and Development Center, Mianyang 621000, China

²Computational Aerodynamics Institute of China Aerodynamics Research and Development Center, Mianyang 621000, China

³LHD, Institute of Mechanics, Chinese Academy of Sciences, Beijing 100190, China

⁴School of Engineering Science, University of Chinese Academy of Sciences, Beijing 100049, China

^{a)} Author to whom correspondence should be addressed: siwei.dong@cardc.cn

ABSTRACT

We report the characteristics of wall shear stress (WSS) and wall heat flux (WHF) from direct numerical simulation (DNS) of a spatially developing zero-pressure-gradient supersonic turbulent boundary layer at a free-stream Mach number $M_\infty = 2.25$ and a Reynolds number $Re_\tau = 769$ with a cold-wall thermal condition (a ratio of wall temperature to recovery temperature $T_w/T_r = 0.75$). A comparative analysis is performed on statistical data, including fluctuation intensity, probability density function, frequency spectra, and space-time correlation. The root mean square fluctuations of the WHF exhibit a logarithmic dependence on Re_τ similar to that for the WSS, the main difference being a larger constant. Unlike the WSS, the probability density function of the WHF does not follow a lognormal distribution. The results suggest that the WHF contains more energy in the higher frequencies and propagates downstream faster than the WSS. A detailed conditional analysis comparing the flow structures responsible for extreme positive and negative fluctuation events of the WSS and WHF is performed for the first time, to the best of our knowledge. The conditioned results for the WSS exhibit closer structural similarities with the incompressible DNS analysis documented by Pan and Kwon [“Extremely high wall-shear stress events in a turbulent boundary layer,” *J. Phys.: Conf. Ser.* **1001**, 012004 (2018)] and Guerrero *et al.* [“Extreme wall shear stress events in turbulent pipe flows: Spatial characteristics of coherent motions,” *J. Fluid Mech.* **904**, A18 (2020)]. Importantly, the conditionally averaged flow fields of the WHF exhibit a different mechanism, where the extreme positive and negative events are generated by a characteristic two-layer structure of temperature fluctuations under the action of a strong Q4 event or a pair of strong oblique vortices. Nevertheless, we use the bi-dimensional empirical decomposition method to split the fluctuating velocity and temperature structures into four different modes with specific spanwise length scales, and we quantify their influence on the mean WSS and WHF generation. It is shown that the mean WSS is mainly related to small-scale structures in the near-wall region, whereas the mean WHF is associated with the combined action of near-wall small-scale structures and large-scale structures in the logarithmic and outer regions.

Published under an exclusive license by AIP Publishing. <https://doi.org/10.1063/5.0079230>

I. INTRODUCTION

Owing to their fundamental importance in a wide range of practical flow configurations, turbulent boundary layers (TBLs) have been extensively studied in the last three decades. Even though considerable progress has been made in the supersonic regime,^{1–6} a more profound understanding of the wall-flow variables beneath compressible turbulent boundary layers is necessary, especially regarding the wall shear stress (WSS) and wall heat flux (WHF). An accurate prediction of skin friction and heat-transfer rates is of great engineering interest,

particularly for drag reduction techniques and the efficient design of thermal protection systems.

A considerable number of experimental and numerical studies have been conducted to improve understanding of the statistics and structure of WSS fluctuations. The logarithmic dependence of the streamwise and spanwise components of the scaled mean WSS fluctuations on the Reynolds number has been well established by laser Doppler anemometry experiments⁷ and direct numerical simulation (DNS) of channel flows^{8,9} and turbulent boundary layers.^{10,11}

The numerical data of Hu *et al.*⁹ suggested that the WSS spectra collapsed under viscous scaling for $Re_\tau \geq 360$. In experiments on a thick axisymmetric turbulent boundary layer on a cylinder, Wietrzak and Lueptow¹² observed that the effect of transverse curvature reduced the low-frequency energy in the spectrum for fluctuating WSS. Using a two-point space–time correlation, Jeon *et al.*¹³ found that streamwise WSS fluctuations in a turbulent channel flow at $Re_\tau = 180$ propagated at a speed of $0.53U_\infty$, and Daniel *et al.*¹¹ revealed that the convection velocity followed a clear decreasing trend with increasing Reynolds number. Taking advantage of the high resolution of the micro-pillar shear stress sensor (MPS³), Grosse and Schröder¹⁴ exactly captured characteristic dimensions of the WSS distribution in turbulent duct flows. That experimental study confirmed the findings of Brücke¹⁵ that the spanwise component of the WSS exhibited wave-like patterns, as well as revealing strong spanwise meandering in the low- and high-shear regions. In a follow-up work, Nottebrock *et al.*¹⁶ used the MPS³ to investigate the WSS distribution in an adverse-pressure-gradient turbulent boundary layer. Recently, Tong *et al.*¹⁷ employed DNS to analyze the effect of expansion on the spatial structures of streamwise and spanwise WSS fluctuations in supersonic turbulent boundary layers and suggested that the spanwise meandering of the fluctuating WSS was significantly suppressed downstream of the expansion. Regarding the fluctuating WHF in wall-bounded turbulent flows, the available data in the literature are very scarce, and there is no consensus on the statistics and structure of WHF fluctuations in supersonic turbulent boundary layers.

One purpose of the present study is to investigate coherent flow structures related to extreme WSS and WHF events. Remarkable advances in the understanding of extreme WSS events have been made in the past few decades, even though the associated intermittency behavior and its relationship to the velocity structure inside the turbulent boundary layer are not yet fully understood. For example, Sheng *et al.*,¹⁸ through a conditional analysis of concurrently measured WSS and the corresponding three-dimensional velocity fields in the inner part of a square duct channel flow at $Re_\tau = 1470$, have identified two distinct types of buffer layer structures: (i) single and paired streamwise vortices, which contribute to the existence of the region with high WSS; (ii) paired streamwise vortices and hairpin-like structures located in the inner layer, which are responsible for extreme negative (EN) WSS events. Similarly, Pan and Kwon¹⁹ numerically investigated the conditionally averaged flow fields around extreme positive (EP) WSS events in a DNS turbulent boundary layer at $Re_\tau = 1500$. The extreme WSS events were detected under a strong fingerlike Q4 event associated with the outer-layer positive large-scale motions and generated by a splattering of high-speed fluids in the near-wall region. This is consistent with conditioned data from hot-film shear sensors together with hot-wire probes in experiments by Hutchins *et al.*,²⁰ who identified the influence of outer very-large-scale motions on positive and negative WSS fluctuations. Further, Gomit *et al.*²¹ divided the histogram of the measured large-scale WSS into four equal quartiles and found that the conditioned flows above the extreme negative WSS events carried a larger amount of Reynolds shear stress than those of the extreme positive WSS events. More recently, Guerrero *et al.*²² have proposed a three-dimensional model to conceptualize the flow dynamics related to extreme WSS events in turbulent pipe flows. Their conditional analysis resulted in two observations about WSS events: the extreme positive WSS regions were

generated by an energetic quasi-streamwise vortex at the buffer layer, and an identifiable oblique vertical structure was clearly found above the backflow events. While the majority of published experimental and numerical studies of extreme WSS events concern incompressible wall-bounded turbulent flows, much less attention has been paid to extreme WSS and WHF events in compressible flows, and a complete picture of the associated coherent structures is still unclear. We are therefore motivated to make one contribution to solving this problem, with our main aim being to examine whether the phenomena reported in the literature for extreme WSS events in the incompressible regime are equally associated with compressible extremes WSS and WHF events. In the present work, we numerically investigate, for the first time to our knowledge, extreme WHF events and related flow features in a supersonic turbulent boundary layer.

The first investigation of mean skin friction generation dates back to the period when Fukagata *et al.*²³ used successive triple integrations of the incompressible mean streamwise momentum equation to derive a simple relation quantifying the contribution of the Reynolds shear stress to the generation of mean skin friction in three canonical wall-bounded turbulent flows, which is frequently quoted as the Fukagata–Iwamoto–Kasagi (FIK) identity. Inspired by the theoretical work of Peet and Sagaut,²⁴ Bannier *et al.*²⁵ proposed an extension of the FIK identity to investigate the effect of wavy riblets on the wall friction. Modesti *et al.*²⁶ derived a generalized version of the FIK identity for duct flows with arbitrary shape to quantify the influence of cross-stream convection on the WSS. Kametani *et al.*²⁷ carried out a comparative study of the dominant terms in the FIK identity in a turbulent boundary layer with and without uniform blowing/suction. Despite the encouraging results obtained from these works, there are still two major questions concerning the FIK identity, namely, a lack of interpretation of the successive triple integrations used and the absence of any physically informed explanation for the linearly weighted Reynolds shear stress. In particular, it was the remarkable work by Renard and Deck²⁸ that overcame some drawbacks of the FIK identity by performing a theoretical derivation of the mean streamwise kinetic energy budget in an absolute reference frame, hereinafter referred to as the Renard–Deck (RD) identity. In their study, the mean skin friction was decomposed into three clearly physically identified terms: direct viscous dissipation, turbulence kinetic energy (TKE) production, and spatial growth. Later, Li *et al.*²⁹ and Fan *et al.*³⁰ generalized the RD identity to compressible flows and used it to investigate the Reynolds number and Mach number dependences and scaling of the contributing terms. To date, the RD identity has been applied successfully to a wide range of complex flows, such as reflected shock interactions,³¹ supersonic expansion corners with shock impingement,³² and adverse-pressure-gradient turbulent boundary layers.³³ Regarding mean WHF generation, only a limited number of studies are available in the literature, and the influence of coherent structures on the generation process is much less understood. Li *et al.*²⁹ recently derived an exact relationship to relate the WHF to the skin friction generation process in compressible turbulent channel flows and suggested that the wall heat transfer might be related to molecular viscous dissipation and TKE production. However, following the approach of Renard and Deck,²⁸ Sun *et al.*³⁴ decomposed the wall heat flux in a hypersonic transitional boundary layer at $M_\infty = 6.0$ by integrating the total energy equation under the reference absolute frame and found that the positive component associated with the

work of the Reynolds stresses and the negative component associated with turbulent transport of heat were predominant in the WHF generation. In the present study, we fill this gap by extending the previous work by Li *et al.*²⁹ and Sun *et al.*³⁴ and applying the bi-dimensional empirical mode decomposition (BEMD) method used by Cheng *et al.*³⁵ to identify the fluctuation structures with specific spanwise length scales and to quantify their contributions to mean WSS and WHF generation in a supersonic turbulent boundary layer.

The remainder of this paper is structured as follows. In Sec. II, the DNS of the spatially developing supersonic turbulent boundary is briefly introduced, including the numerical methodology used and the validation of the DNS database. The WSS and WHF are focused on in Sec. III, through an analysis of statistical properties, the flows associated with extreme events, and a scale-based decomposition. Finally, concluding remarks are presented in Sec. IV.

II. SIMULATION SETUP

A. Numerical methodology and inflow conditions

In the present simulation, the governing equations are the full three-dimensional compressible conservative Navier–Stokes equations for a perfect gas in Cartesian coordinates (x, y, z) , which are non-dimensionalized by inflow parameters. The strain-rate tensor S_{ij} and the dynamic viscosity coefficient μ are related to the viscous stress tensor σ_{ij} via the constitutive relation for a Newtonian fluid, and Fourier's law of heat conduction is used to calculate the heat flux vector q_j . The thermodynamic variables are assumed to obey the ideal gas equation of state, and the dynamic viscosity coefficient is related to the temperature through Sutherland's law. The specific heat capacity ratio and the molecular Prandtl number are taken as $\gamma = 1.4$ and $Pr = 0.71$, where the thermal conductivity is $k = \mu C_p / Pr$, with C_p being the specific heat capacity of gas at a constant pressure. More detailed descriptions of the governing equations can be found in Tong *et al.*³⁶

We use an open-source high-order finite-difference flow solver, Openfd-SC, to directly solve the governing equations without any modeling. This code has been extensively used in previous DNS studies of compressible flows, involving compression ramps,^{37,38} reflected interactions,³⁹ supersonic flat-plate turbulent boundary layers (TBLs),⁴⁰ and it has been thoroughly validated that the compressible turbulence can be accurately captured. For the spatial derivatives, a fourth-order weighted essentially non-oscillatory (WENO) scheme, proposed by Martin *et al.*⁴¹ and Wu and Martin,⁴² is used to calculate the convective flux terms. The present scheme uses a symmetric collection of candidate stencils and a set of optimized WENO weights in the linear part of the original WENO scheme introduced by Jiang and Shu⁴³ to maximize bandwidth resolution, and the method of limiters is used to further reduce numerical dissipation. A standard eighth-order central difference scheme is used to calculate the viscous flux terms. For the time integration, the third-order total variation diminishing Runge–Kutta scheme of Gottlieb and Shu⁴⁴ is applied.

The selected free-stream inflow conditions are similar to the DNS of Pirozzoli *et al.*⁴⁵ in the case of a supersonic zero-pressure-gradient flat-plate TBL, including a nominal free-stream Mach number of $M_\infty = 2.25$, a free-stream static temperature of $T_\infty = 169.44$ K, and a unit free-stream Reynolds number of $Re_\infty/\text{mm} = 2.5 \times 10^4$. The inflow turbulence is generated using the laminar-to-turbulent transition method proposed by Pirozzoli *et al.*⁴⁵ with the wall blowing and suction region set downstream of the inflow laminar boundary layer.

To induce the transition, the imposed wall-normal velocity fluctuations at the wall are similar to the disturbances suggested by Pirozzoli *et al.*⁴⁵ and Fang *et al.*,⁴⁶ whereby there are two temporal modes, two spatial modes in the streamwise direction, and ten spatial modes in the spanwise direction. As confirmed by Fang *et al.*⁴⁶ and Gao *et al.*,⁴⁰ no extra mass flux is introduced into the boundary layer due to the zero net flow rate at the wall.

B. Computation overview

The size of the computational domain is $L_x \times L_y \times L_z = 155\delta_0 \times 10\delta_0 \times 8.75\delta_0$, where L_x , L_y , and L_z are the extents in the streamwise (x), wall-normal (y), and spanwise (z) directions, respectively, and the compressible inflow laminar boundary layer thickness at the domain inlet ($x = 0$) is about $\delta_0 = 0.508$ mm (based on the 99% free-stream velocity; see Fig. 2). Unless otherwise stated, the spatial coordinates in the following analysis are normalized by δ_0 . As sketched in Fig. 1, a structured Cartesian mesh consisting of $N_x \times N_y \times N_z = 2105 \times 400 \times 340$ grid points is used to discretize the flow domain. Following Pirozzoli *et al.*,⁴⁵ the mesh in the streamwise direction is progressively refined in the transition region extending from $x = 0$ to $x = 100$ (for a total of 400 grid points) and quickly coarsened in the fringe region $x > 150$. A total of 1595 grid points are equally distributed in the turbulent region $100 < x < 150$, corresponding to a uniform grid distribution of $\Delta x = 0.031$. In the wall-normal direction, the grid points are clustered toward the wall using a hyperbolic tangent mapping, with 280 grid points located inside the boundary layer, whereby the grid spacings at the wall and at the edge of TBL ($x = 125$) are $\Delta y_w = 0.002$ and $\Delta y_e = 0.02$, respectively. In the spanwise direction, the grid spacing is kept at a constant value of $\Delta z = 0.026$. In wall units calculated at $x = 125$, the non-dimensionalized spatial resolutions of the grid in the well-resolved turbulent region are $\Delta x^+ = 8.5$, $\Delta y_w^+ = 0.55$, $\Delta y_e^+ = 5.5$, and $\Delta z^+ = 7.15$, respectively, which are comparable to those in recent DNS studies of compressible TBL by Bernardini and Pirozzoli⁴⁷ and Wu *et al.*⁴⁸ Throughout this paper, the superscript “+” stands for normalization by wall viscous scales in the TBL region, and the subscripts “e” and “w” denote quantities calculated at the wall and the edge of the TBL, respectively.

A steady inflow laminar profile (see Fig. 2), obtained from an auxiliary DNS simulation under the same inflow conditions, is prescribed at the inlet of the domain. Nonreflecting boundary conditions are prescribed at the outlet and the upper far-field boundary of the domain to avoid reflection of disturbances back into the domain. The selected spanwise width is sufficiently large, and periodic boundary conditions are used in the spanwise direction. At the wall, no-slip boundary conditions are used, with a constant wall temperature of $T_w = 254.16$ K. Under the inflow conditions considered here, the wall-to-recovery-temperature ratio T_w/T_r is about 0.75, where T_r is the wall recovery temperature, indicating that an isothermal cold wall is prescribed in the present study. As shown in Fig. 2(b), the unsteady

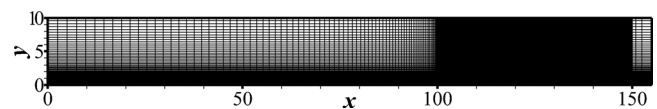


FIG. 1. Sketch of the computational mesh in the x – y plane. The grid is plotted only every tenth point and fifth point in the x and y directions, respectively.

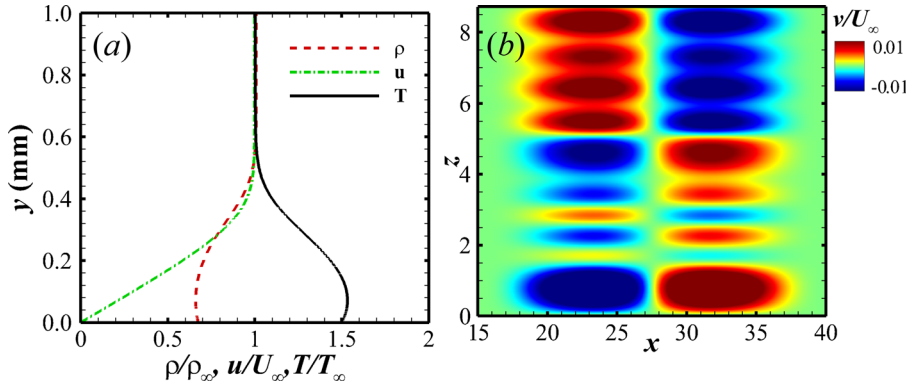


FIG. 2. (a) Profile of inflow laminar boundary layer. (b) Visualization of wall-normal velocity disturbances in the region of blowing and suction.

wall-normal velocity disturbances, expressed as $v_{bs} = Af_{bs}(x)g_{bs}(z)h_{bs}(t)$ and

$$\begin{aligned}
 f_{bs}(x) &= \frac{4}{\sqrt{27}} \sin(2\pi x_{bs}) [1 - \cos(2\pi x_{bs})], \\
 g_{bs}(z) &= \sum_{l=1}^{l_{\max}} 0.8^{l-1} g_0 \sin[2\pi l(z_{bs} + \phi_l)], \\
 h_{bs}(t) &= \sum_{m=1}^{m_{\max}} 0.8^{m-1} h_0 \sin[2\pi m(\varpi t + \phi_m)], \\
 g_0 &= 1 / \sum_{l=1}^{l_{\max}} 0.8^{l-1}, \quad h_0 = 1 / \sum_{m=1}^{m_{\max}} 0.8^{m-1}, \\
 x_{bs} &= \frac{x - x_a}{x_b - x_a}, \quad z_{bs} = \frac{z}{L_z}
 \end{aligned} \tag{1}$$

are only enforced in the blowing and suction region ($15 < x < 40$ and $0 < z < 8.75$). Here, $l_{\max} = 10$, $m_{\max} = 5$, $x_a = 15$, $x_b = 40$, and ϕ_l and ϕ_m denote random numbers between 0 and 1. To accelerate the transition in the current simulation, we chose a disturbance amplitude $A = 0.15U_\infty$ and a basic frequency of the disturbances $\varpi = 0.157U_\infty/\delta_0$, both of which larger than those of Pirozzoli *et al.*⁴⁵ and Fang *et al.*⁴⁶

In the present spatial simulation, as the disturbed boundary layer develops downstream, fully developed turbulence is finally obtained after $x > 100$. It can be seen from Fig. 3 that inclined and highly intermittent turbulent bulges are clearly observed in the outer region of the boundary layer, and the streamwise velocity flow field in the near-wall region is mainly characterized by alternating low- and high-speed streaks in the spanwise direction, consistent with previous numerical and experimental observations of a supersonic flat-plate TBL. After a washout time of about $200U_\infty/\delta_0$ (or three flow-through times, FTTs), the effect of the initial transient solution is negligible and a statistical stationary state is attained. Here, we choose the flow data over a narrow streamwise range of $[x_0 - 10, x_0 + 10]$ ($x_0 = 125$) to calculate the mean and statistical quantities in the following analysis. At $x = 125$, the boundary layer thickness based on 99% free-stream velocity is estimated as $\delta = 1.27$ mm, and the displacement thickness and momentum thickness are $\delta^*/\delta = 0.204$ and $\theta/\delta = 0.073$, respectively. Correspondingly, the representative Reynolds numbers are $Re_\theta = \rho_\infty U_\infty \theta / \mu_\infty = 2318$, $Re_{\delta^*} = \rho_\infty U_\infty \delta^* / \mu_\infty = 2571$, and $Re_\tau = \rho_w u_\tau \delta / \mu_w = 769$. It is important to note that the boundary layer

parameters are changed by less than 2% over the selected streamwise region, suggesting that the effect of the spatial growth of the TBL on the following statistical properties is negligible.

C. Validation of DNS data

For the purpose of validation, we quantitatively compare the turbulence statistics at a selected location $x = 125$, including the van Driest transformed mean streamwise velocity U_{vd}^+ , the density-scaled Reynolds stress components R_{ij} , the turbulence kinetic energy budget, and the power spectral density (PSD) of the wall pressure fluctuations, with the reference DNS and experimental data for a flat-plate TBL at comparable Reynolds numbers. In the results that follow, a bar and a tilde indicate the Reynolds average and the Favre (density-weighted) average, respectively, with a prime and a double prime for the corresponding fluctuations, and the mean values are calculated by the average in the spanwise direction and in time.

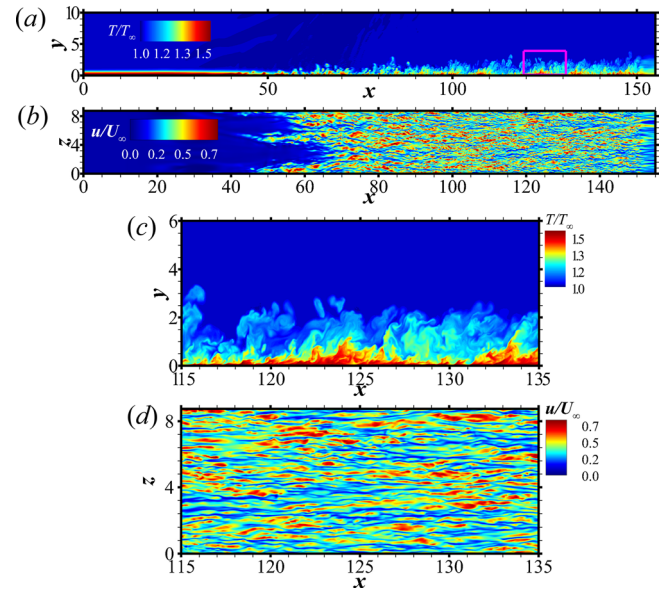


FIG. 3. (a) Instantaneous temperature flow field in the x - y plane. (b) Instantaneous streamwise velocity flow field in the x - z plane at $y^+ = 10$. (c) and (d) Enlargement of the zones marked with pink boxes in (a) and (b).

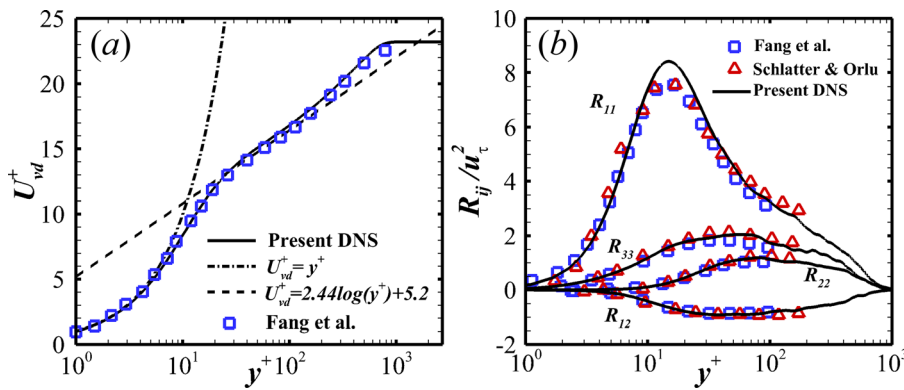


FIG. 4. (a) Profile of the van Driest transformed mean velocity in inner scaling. (b) Distribution of the density-scaled Reynolds stress components.

The mean velocity profile, as reported in Fig. 4(a), is in good agreement with the compressible DNS data of Fang *et al.*,⁴⁶ and follows the incompressible logarithmic law with von Kármán constants $\kappa = 0.41$ and $C = 5.2$ in the logarithmic region $30 < y^+ < 100$ and the linear viscous sublayer law up to $y^+ < 6$. According to Morkovin’s hypothesis,⁴⁹ the computed Reynolds stress components in Fig. 4(b) are scaled by the mean density profile to account for the compressibility effect. As expected, a good collapse with the incompressible and compressible flat-plate DNS results of Schlatter and Örlü⁵⁰ and Fang *et al.*⁴⁶ is observed, where the peak streamwise turbulence intensity occurs at $y^+ \approx 15$, with the peak value being slightly larger than those of the reference DNS owing to the different Reynolds number and isothermal wall condition.

Figure 5(a) shows the budget terms of the turbulence kinetic energy K , where the compressible transport equation for K is defined as $\partial \bar{\rho} K / \partial t = C_k + T_k + P_k + V_k - \varepsilon + M_k$. Here, C_k , T_k , P_k , V_k , ε , and M_k denote the mean advection contribution, the turbulent transport term, the production term associated with mean velocity gradients, the viscous diffusion term, the viscous dissipation term, and the direct compressibility effect, respectively. A more detailed explicit expression for the budget terms can be found in Tong *et al.*³⁷ The figure highlights the close similarities with the compressible DNS results of Fang *et al.*⁴⁶ and Pirozzoli *et al.*,⁵¹ where P_k attains a maximum in the buffer layer at $y^+ \approx 12$. Consistent with previous findings for a canonical zero-pressure-gradient supersonic TBL, the contributions of C_k and M_k can be neglected owing to the rather small amplitude, while

the viscous dissipation ε in the near-wall region is mainly balanced by the viscous diffusion V_k , in contrast to the relative balance between the production term P_k and the viscous dissipation ε in the outer layer. The frequency spectrum of the wall pressure fluctuations in inner scaling is given in Fig. 5(b) as a function of the angular frequency ω and is carefully validated against previous experimental data of Gravante *et al.*⁵² at $Re_\tau = 715$ and Farabee and Casarella⁵³ at $Re_\tau = 1165$. It can be seen that the spectrum at high frequencies varies like ω^{-5} , owing to the contributions of near-wall motions.

III. RESULTS AND DISCUSSION

In the following analysis, the wall shear stress and heat flux, defined as

$$\tau(x, y, z, t) = \mu \frac{\partial u(x, y, z, t)}{\partial y} \Big|_w \quad \text{and} \quad q(x, y, z, t) = k \frac{\partial T(x, y, z, t)}{\partial y} \Big|_w, \quad (2)$$

are fully time-resolved and are sampled at a short constant time interval of $0.6U_\infty/\delta_0$. To guarantee statistical convergence, a total of 15 000 instantaneous fields of WSS and WHF spanning a long time period of approximately $600U_\infty/\delta_0$ (or 11 FTTs) are equally collected in the region $120 < x < 130$ and $0 < z < 8$.

To provide an overall organization of the fluctuation fields, in Fig. 6 we show instantaneous snapshots of the WSS and WHF fluctuations. The fluctuating WSS, shown in Fig. 6(a), which resembles very

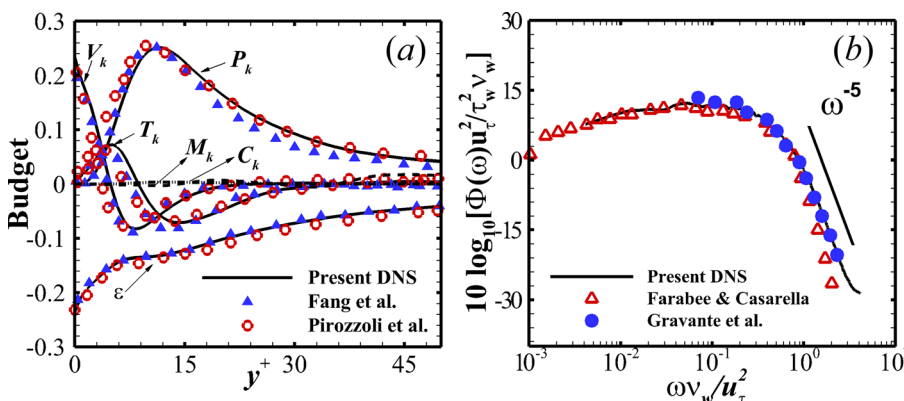


FIG. 5. (a) Turbulence kinetic energy budget. The individual terms are normalized by $\rho_w u_\tau^2 / \nu_w$. (b) Wall pressure frequency spectrum in inner scaling.

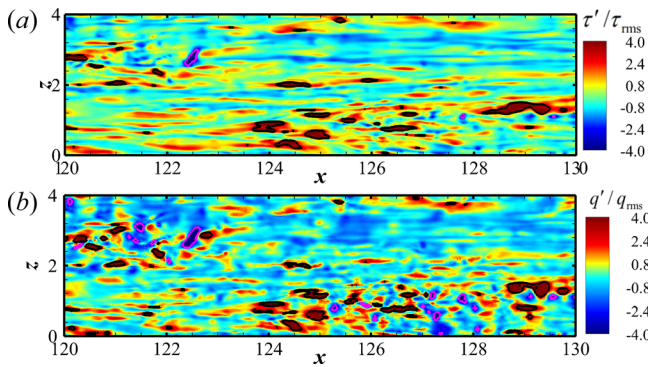


FIG. 6. Instantaneous flow fields of fluctuations: (a) WSS; (b) WHF. The black and pink lines represent $\pm 3\tau_{rms}$ in (a) and $\pm 3q_{rms}$ in (b).

closely the WSS distributions of an incompressible turbulent duct flow obtained by Grosse and Schröder¹⁴ and of a low-Reynolds-number channel flow obtained by Jeon *et al.*,¹³ is organized into alternating elongated streamwise streaks of positive WSS and negative WSS, exhibiting close similarities with the typical streaky pattern of velocity fields previously observed inside incompressible and compressible boundary layers. In Fig. 6(b), the fluctuating WHF, which is elongated in the streamwise direction, is clearly seen. A notable difference is found in the characteristic length scales in the streamwise and spanwise directions. Careful observation shows that the streamwise characteristic length scale is dramatically decreased compared with that of the WSS fluctuations, whereas the spanwise characteristic length scale is slightly increased, which will be quantitatively discussed in Sec. III A. Another important difference is the occurrence probability of extreme events, especially extremely negative events. Following Guerrero *et al.*,²² events with $\tau' < -3\tau_{rms}$ or $q' < -3q_{rms}$ are defined as extreme negative (EN) events, while events with $\tau' > 3\tau_{rms}$ or $q' > 3q_{rms}$ are defined as extreme positive (EP) events throughout this paper. Here, τ_{rms} and q_{rms} denote the root mean square (rms) value of the WSS and WHF fluctuations, respectively. It is clear that EN events are much more common in the WHF fluctuations than in the WSS fluctuations.

A. Statistical properties

The rms fluctuations of WSS and WHF (τ_{rms}^+ and q_{rms}^+), normalized by the local mean values, are shown in Fig. 7 as functions of Re_τ

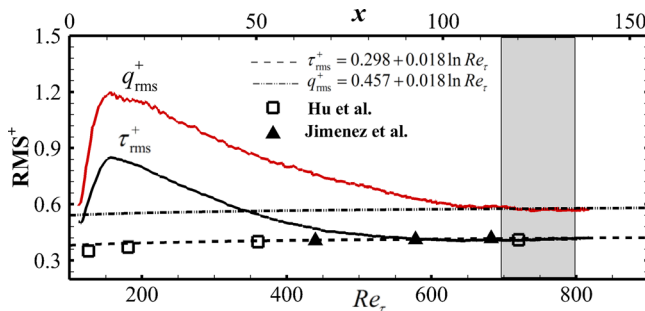


FIG. 7. The rms fluctuations of the WSS and WHF as functions of Re_τ and x . The rms values are normalized by the local mean values, and the gray shading indicates the turbulent region.

and x , together with the incompressible channel DNS data of Hu *et al.*⁹ and Jimenez *et al.*⁵⁴ and the correlation proposed by Örlü and Schlatter¹⁰

$$\tau_{rms}^+ = 0.298 + 0.018 \ln Re_\tau. \tag{3}$$

Note that the results in the transition region are also included for comparison. For τ_{rms}^+ , the present simulation data in the transition region do not follow the above logarithmic correlation, and the peak value emerges in the blowing and suction region, which is related to the trip methods used in the turbulence generation, as also found in previous DNS of incompressible TBL by Daniel *et al.*¹¹ and Schlatter and Örlü.⁵⁵ After experiencing a rapid decay in the transition region, the computed rms values in the turbulent region ($x > 115$ and $Re_\tau > 700$) compare very well with the logarithmic correlation. For q_{rms}^+ , similar behavior is observed, with the main difference being the larger amplitude of q_{rms}^+ than that of τ_{rms}^+ throughout the computational domain, and the correlation

$$q_{rms}^+ = 0.457 + 0.018 \ln Re_\tau, \tag{4}$$

fits the current WHF fluctuations in the turbulent region with satisfactory agreement, indicating a logarithmic dependence on the Reynolds number. We observe that the curve for q_{rms}^+ has the same logarithmic slope as τ_{rms}^+ but a different constant, similar to the previous findings by Daniel *et al.*¹¹ for the spanwise WSS fluctuations, which can be attributed to the essential differences between the fluctuating streamwise velocity and temperature fields in the near-wall region.

Figure 8(a) compares the probability density functions (PDFs) of the WSS τ^+ and WHF q^+ with a lognormal distribution. Consistent with the work of Daniel *et al.*,¹¹ the PDF of τ^+ displays a positively skewed distribution and shows the nonzero probability of $\tau^+ < 0$, further confirming the existence of backflow. Good agreement with a lognormal distribution is obtained in the central region of the PDF, whereas the extreme tails deviate significantly, in accordance with the previous study by Guerrero *et al.*²² The figure also shows a clear width increment of the PDF tails of q^+ , which is more pronounced in the negative tail, meaning that the skewness is decreased. It is important to notice that the distribution of q^+ does not follow a lognormal distribution, and the occurrence probability of $q^+ < 0$ becomes much higher compared with that of τ^+ . In addition, the PDF of the normalized WSS fluctuations τ' , shown in Fig. 8(b), exhibits good agreement with the supersonic TBL findings of Tong *et al.*¹⁷ at $Re_\theta = 2300$, the incompressible TBL experiments of Nottbrock *et al.*¹⁶ at $Re_\theta = 4420$, the turbulent duct experiments of Grosse and Schröder¹⁴ at $Re_H = 15000$ (based on the duct height), and the channel flow observations of Sreenivasan and Antonia⁵⁶ at $Re_D = 6050$ (based on the channel half-height), except for the considerable differences observed in the left tail. Under such a normalization, it is clear that the PDF of q' agrees well with that of τ' for $-2 < q'/q_{rms} < 4$, whereas large deviations occur only in the extremely negative tail. This figure also helps to explain the sharp decrease in EN events previously observed in Fig. 6, where the probability of $q'/q_{rms} = 3.0$, corresponding to the threshold for the EN events, is about an order of magnitude larger than that of $\tau'/\tau_{rms} = 3.0$.

Figure 9 shows the premultiplied frequency spectra of τ' and q' as functions of the normalized angular frequency $\omega v_w/u_\tau^2$ to determine the energy distribution in frequency space, where the Welch method is used to estimate the power spectral density $\Psi(\omega)$ and the

Downloaded from http://pubs.aip.org/journal/phf/article-pdf/doi/10.1063/5.0079230/16624619/015127_1_online.pdf

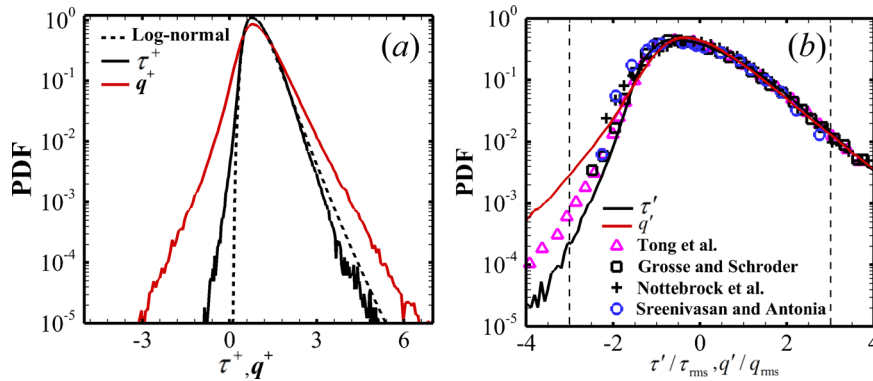


FIG. 8. (a) PDFs of the WSS and WHF, together with a lognormal distribution. (b) PDFs of the WSS and WHF fluctuations, normalized by the rms values. Dashed lines mark the thresholds for extremely positive and negative events.

spectra are averaged in the spanwise direction and normalized with the squares of the mean WSS and WHF, respectively. The WSS spectrum shows good quantitative agreement with the data from the simulations of incompressible TBLs by Daniel *et al.*¹¹ and of channel flow by Hu *et al.*,⁹ when the inner scaling is applied. The peak frequency occurs at $\omega v_w / u_\tau^2 \approx 0.07$, which is very close to the value reported in previous studies. An apparently good collapse between the wall shear stress and heat flux spectrum is only observed at the low-frequency end for $\omega v_w / u_\tau^2 < 0.2$. Importantly, the most notable feature of the WHF spectrum appears to be a strong enhancement of the high-frequency components. For $\omega v_w / u_\tau^2 > 0.1$, the WHF spectrum contains more energy, and the peak frequency is shifted to $\omega v_w / u_\tau^2 \approx 0.5$, which is indicative of the predominance of small-scale, high-frequency dynamics in the WHF field. This behavior is probably linked to the fundamentally different dynamics of temperature streaks and streamwise velocity streaks, since the temperature fluctuations tend to be more isotropic than the streamwise velocity fluctuations, as previously observed by Pirozzoli and Bernardini² in supersonic TBLs.

To single out the structural differences between the WSS field and the WHF field, we show in Fig. 10 the respective two-point

correlation coefficients $C_{\tau\tau}(\Delta x^+, \Delta z^+)$ and $C_{qq}(\Delta x^+, \Delta z^+)$, which are defined as

$$C_{\alpha\alpha}(\Delta x^+, \Delta z^+) = \frac{\overline{\alpha'(x, z, t)\alpha'(x + \Delta x^+, z + \Delta z^+, t)}}{\alpha_{\text{rms}}(x)\alpha_{\text{rms}}(x + \Delta x^+)}, \quad (5)$$

where α represents the fluctuations of τ or q , with Δx^+ and Δz^+ being the streamwise and spanwise spatial separations in wall units. The probe is located at $x = 125$ hereinafter. As found for turbulent duct flow,¹⁴ as well as for compressible and incompressible flat-plate TBLs,^{11,17} the contour for τ' , shown in Fig. 10(a), can be seen to possess a streamwise elongated distribution, reflecting the streaky structure previously observed in Fig. 6, and there are two negative regions flanking both sides of the elongated positive region in the spanwise direction, which is a clear reflection of the spanwise-alternating stripes of the negative and positive WSS fluctuations. The contour for q' is still elongated in the streamwise direction, and a significant decrease in the streamwise coherence and a noticeable increase in the spanwise coherence are highlighted in Fig. 10(b), indicating a reduced anisotropy of the WHF field. For instance, the streamwise and spanwise extents of a correlation value of 0.3 are about $\Delta x^+ = 440$ and $\Delta z^+ = 52$, respectively, for τ' , compared with $\Delta x^+ = 216$ and $\Delta z^+ = 68$ for q' .

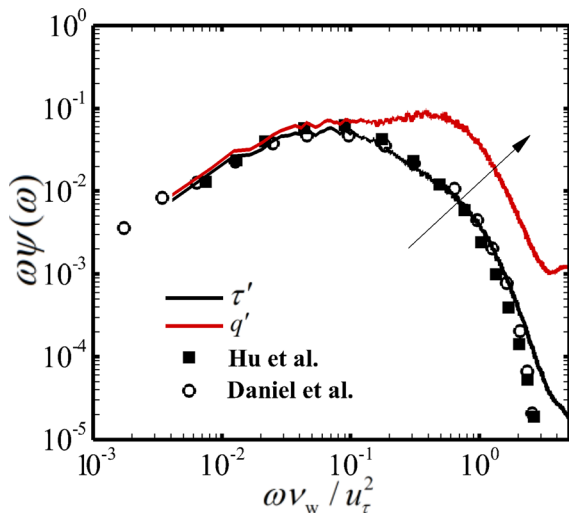


FIG. 9. Premultiplied frequency spectra of WSS and WHF fluctuations. The spectra are normalized by the squares of the respective mean values.

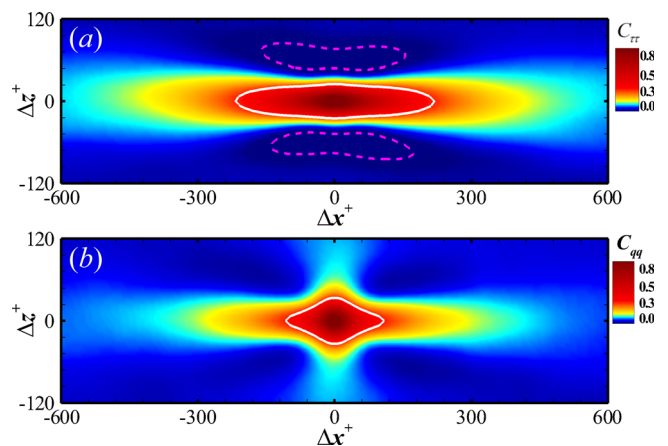


FIG. 10. Contours of the two-point correlation coefficients: (a) $C_{\tau\tau}(\Delta x^+, \Delta z^+)$; (b) $C_{qq}(\Delta x^+, \Delta z^+)$. Solid white lines and dashed pink lines correspond to correlation values of 0.3 and -0.03 , respectively.

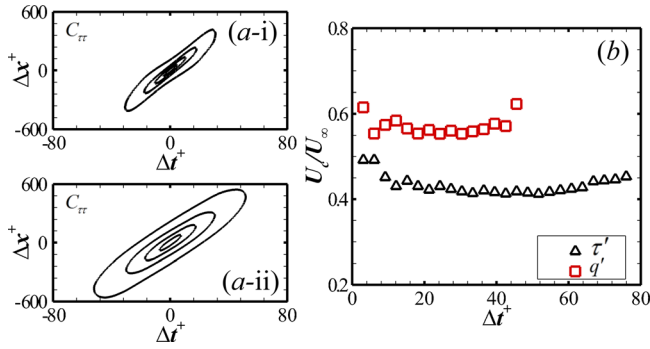


FIG. 11. (a) Isolines of the space-time correlation coefficients $C_{\tau\tau}(\Delta x^+, \Delta t^+)$ and $C_{qq}(\Delta x^+, \Delta t^+)$. Four contour levels are shown from 0.3 to 0.9, with increments of 0.2. (b) Convection velocity U_c/U_∞ as a function of time delay Δt^+ .

This finding quantitatively supports the visualization analysis in Fig. 6. It is worth noting that the negatively correlated region in Fig. 10(b) appears to be less evident and the fluctuating WHF correlates positively over a distance of $\Delta z^+ = 240$ at $\Delta x^+ = 0$, suggesting that the spanwise-alternating streaky pattern become less significant in the WHF field.

We close this section with an analysis of the space-time correlation coefficients of the WSS and WHF, $C_{\tau\tau}(\Delta x^+, \Delta t^+)$ and $C_{qq}(\Delta x^+, \Delta t^+)$, presented in Fig. 11, which are defined as

$$C_{\alpha\alpha}(\Delta x^+, \Delta t^+) = \frac{\overline{\alpha'(x, z, t)\alpha'(x + \Delta x^+, z, t + \Delta t^+)}}{\alpha_{rms}(x)\alpha_{rms}(x + \Delta x^+)}, \quad (6)$$

where α represents the fluctuations of τ or q , with Δt^+ and Δx^+ being the time delay and the streamwise spatial separation in wall units. As expected, both maps in Fig. 11(a) are dominated mainly by a forward-leaning behavior, as a consequence of strong downstream propagation of the fluctuations, consistent with previous observations of WSS fluctuations in turbulent channel flows by Jeon *et al.*¹³ and

Park and Moin.⁵⁷ However, the map shape of C_{qq} is highly skewed and becomes more narrow, resulting in a larger inclination compared with $C_{\tau\tau}$. This behavior can be better understood from Fig. 11(b), where the convective velocity U_c is presented as a function of Δt^+ . Following Duan *et al.*,⁵⁸ U_c is defined as the ratio $\Delta x^*/\Delta t^*$, with Δx^* being the streamwise position at which the correlation value attains a local maximum for a given time delay Δt^* . The convective velocity of τ' is weakly dependent on the time delay, where $U_c = 0.42U_\infty$ to $0.49U_\infty$, which is slightly lower than the $U_c = 0.53U_\infty$ of Jeon *et al.*¹³ at $Re_\tau = 180$ and the $U_c = 0.52U_\infty$ to $0.56U_\infty$ of Daniel *et al.*¹¹ at $Re_\theta = 1072$. This is probably linked to the different Reynolds numbers ($Re_\tau = 769$ and $Re_\theta = 2318$) used in the present study. Previous DNS data of Daniel *et al.*¹¹ suggested a Reynolds number dependence, with the propagation speed of the WSS fluctuations decreasing for higher Reynolds number. Moreover, the distribution of the convection velocity of q' is very similar to that of τ' , but q' propagates downstream with larger speeds $U_c = 0.55U_\infty$ to $0.62U_\infty$. Combined with the peak frequencies shown in Fig. 9 and the computed convection velocity, the most energetic scale is about $\Lambda_\tau^+ \approx 900$ for τ' and $\Lambda_q^+ \approx 200$ for q' . It is conjectured that the higher convection velocity of the fluctuating WHF might be associated with the smaller characteristic length scales, consistent with the two-point correlation analysis in Fig. 10.

B. Flow associated with extreme events

In this subsection, we aim to relate the flow fields to the previously detected extreme events of τ' and q' in Fig. 6 by means of conditional average, similar to the methods of Pan and Kwon¹⁹ and Guerrero *et al.*²² Specifically, an averaging box, covering $-300 < \Delta x^+ < 300$, $0 < y^+ < 450$, and $-150 < \Delta z^+ < 150$, has been selected to condition on an extreme event, which is placed at $\Delta x^+ = 0$, $y^+ = 0$, and $\Delta z^+ = 0$. The following conditionally averaged fields are based on 600 snapshots of velocity and temperature fields, where the numbers of EP events in τ' and q' are nearly the same, about 1.7×10^6 , and the number of EP events in τ' is about 1.9×10^4 , much smaller than those

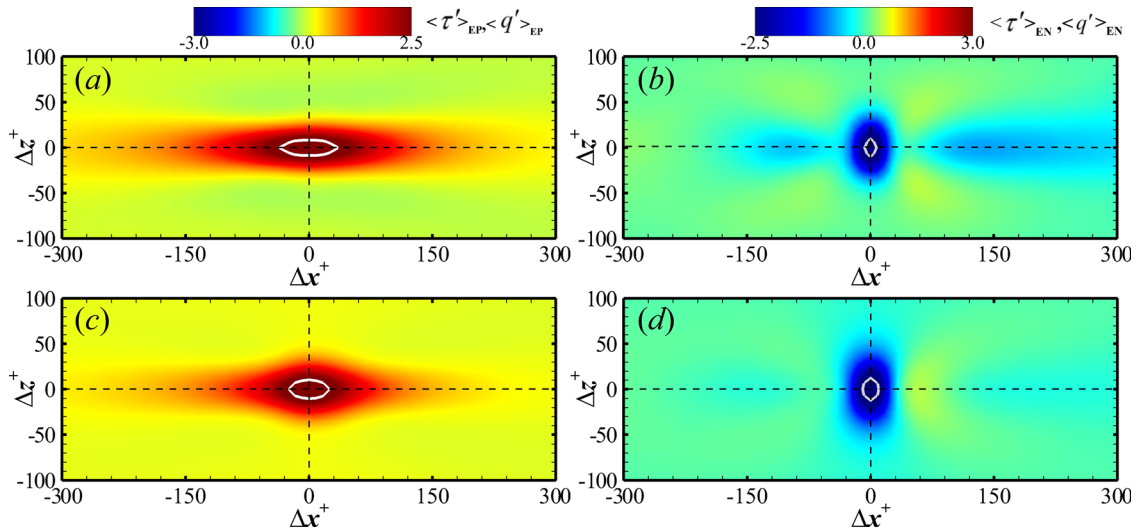


FIG. 12. Conditionally averaged τ' and q' around an extreme event at $\Delta x^+ = 0$ and $\Delta z^+ = 0$: (a) $\langle \tau' \rangle_{EP}$; (b) $\langle \tau' \rangle_{EN}$; (c) $\langle q' \rangle_{EP}$; (d) $\langle q' \rangle_{EN}$. White solid lines in (a) and (c) denote $\langle \tau' \rangle_{EP} = 3$ and $\langle q' \rangle_{EP} = 3$, respectively. Gray solid lines in (b) and (d) denote $\langle \tau' \rangle_{EN} = 3$ and $\langle q' \rangle_{EN} = 3$, respectively.

in q' , which is about 2.9×10^5 . A sensitivity study has been performed by decreasing the flow samples, and no essential changes have been found, indicating that statistical independence is obtained in the present study.

Figures 12(a) and 12(b) show the conditionally averaged τ' around an EP event and an EN event, defined as $\langle \tau' \rangle_{EP}$ and $\langle \tau' \rangle_{EN}$, respectively, while the conditionally averaged q' is reported in Figs. 12(c) and 12(d) as $\langle q' \rangle_{EP}$ and $\langle q' \rangle_{EN}$. Throughout this section, $\langle \rangle_{EP}$ and $\langle \rangle_{EN}$ represent the conditional average fields associated with an EP event and an EN event, respectively. In Figs. 12(a) and 12(c), $\langle \tau' \rangle_{EP}$ and $\langle q' \rangle_{EP}$ are both characterized by an elliptical behavior, being elongated in the streamwise direction and resembling very closely the observations in previous DNS studies.^{19,22} By contrast, a spanwise elongated elliptical region of high magnitude of $\langle \tau' \rangle_{EN}$ and $\langle q' \rangle_{EN}$ is clearly found in Figs. 12(b) and 12(d), which is different from the round-shaped pattern in a DNS study of EN WSS

fluctuations of a TBL by Pan and Kwon.¹⁹ This difference can be attributed to the detection method used. In the previous study by Pan and Kwon,¹⁹ extreme events only in a round-shaped isolated region with thresholds ($AR \leq 4$ and $r^+ \geq 40$, AR and r^+ are the aspect ratio and the equivalent radius of the isolated region) were conditioned, whereas a single threshold ($\tau' = \pm 3\tau_{rms}$ or $q' = \pm 3q_{rms}$) is used in the present study, without any structural limitation. Moreover, although the size of $\langle \tau' \rangle_{EP}$ based on the threshold of 3.0, which is approximately 70×20 wall units in the Δx^+ and Δz^+ directions, is essentially larger than the approximate size of 30×10 wall units found by Guerrero *et al.*²² in an incompressible turbulent pipe flow, the ratio $\Delta x^+/\Delta z^+$ is nearly the same. Compared with $\langle \tau' \rangle_{EP}$, the ratio $\Delta x^+/\Delta z^+$ of $\langle q' \rangle_{EP}$ in Fig. 12(c) is significantly decreased, as a consequence of a large decrease in the streamwise extent ($\Delta x^+ = 48$) and a slight increase in the spanwise

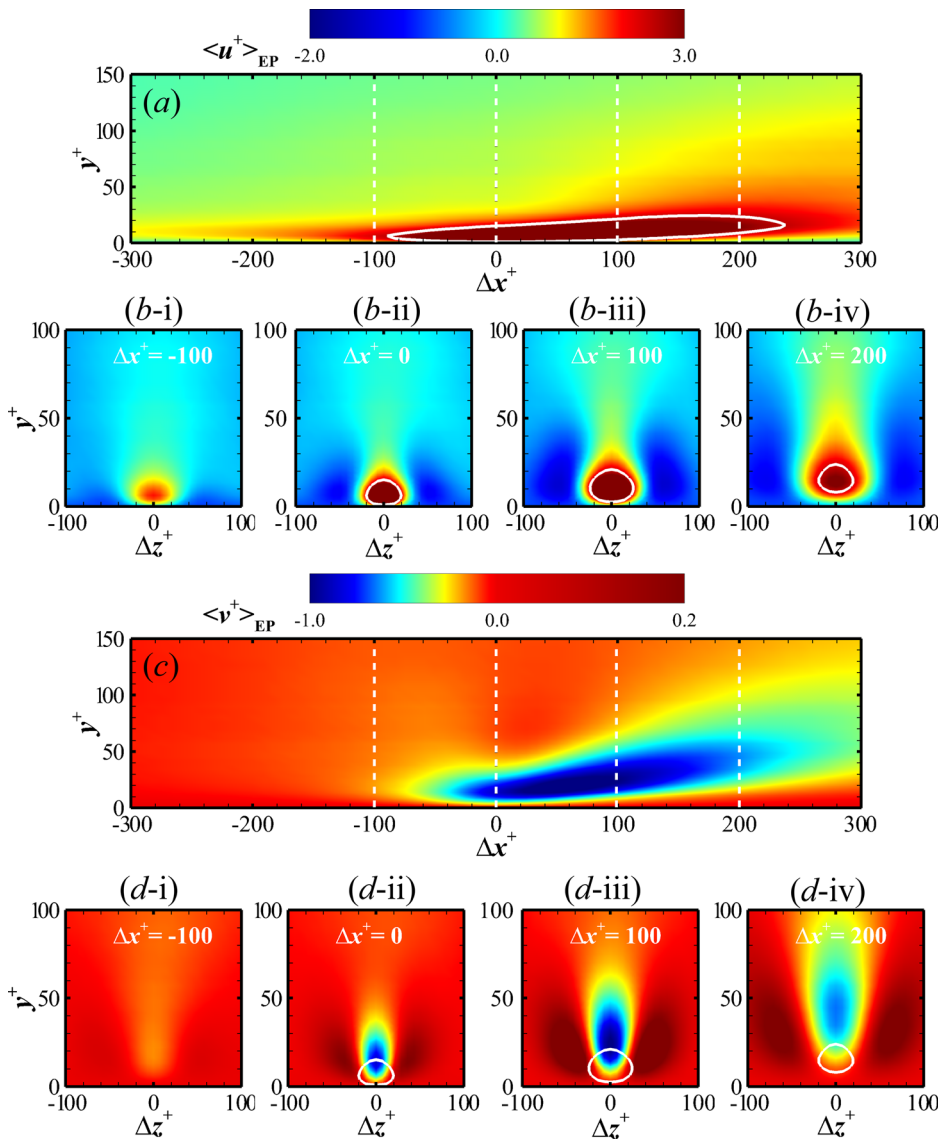


FIG. 13. Conditionally averaged velocity fluctuations associated with an EP event of τ' at $\Delta x^+ = 0$ and $\Delta z^+ = 0$. (a) and (c) Streamwise and wall-normal velocities in the $(\Delta x^+, y^+)$ plane at $\Delta z^+ = 0$. (b) and (d) Streamwise and wall-normal velocities in the $(\Delta z^+, y^+)$ plane at four streamwise locations marked by dashed lines in (a) and (c). White solid lines in (a), (b), and (d) denote $(u^+)_{EP} = 2.5$.

extent ($\Delta z^+ = 21$). In addition, we observe that the spanwise sizes of $\langle \tau' \rangle_{EN}$ and $\langle q' \rangle_{EN}$ in Figs. 12(b) and 12(d) are very close to those of $\langle q' \rangle_{EN}$ and $\langle q' \rangle_{EN}$, whereas the streamwise sizes become much smaller, $\Delta x^+ = 14$ for $\langle \tau' \rangle_{EN}$ and $\Delta x^+ = 20$ for $\langle q' \rangle_{EN}$, implying the predominance of spanwise coherence.

We first focus on the flow structures associated with EP events by comparing Figs. 13 and 14, where the conditionally averaged fluctuations around an EP event of τ' and an EP event of q' are reported, respectively. Here, Figs. 13(a), 13(c), 14(a), and 14(c) present the conditionally averaged fields in the $(\Delta x^+, y^+)$ plane at $\Delta z^+ = 0$, while Figs. 13(b), 13(d), 14(b), and 14(d) present the fluctuations in the $(\Delta z^+, y^+)$ plane at $\Delta x^+ = -100, 0, 100$, and 200 . Clearly, there is a region of high positive $\langle u^+ \rangle_{EP}$ in Fig. 13(a) and a region of high negative $\langle v^+ \rangle_{EP}$ in Fig. 13(c), both located between $-100 < \Delta x^+ < 240$ and $0 < y^+ < 30$, demonstrating that the EP event of τ' emerges below a

strong Q4 event in the buffer region, as suggested by Guerrero *et al.*²² and Pan and Kown.¹⁹ Figure 13(b) reveals that there exist two regions of negative $\langle u^+ \rangle_{EP}$, flanking the central high positive $\langle u^+ \rangle_{EP}$. Accordingly, two regions of positive $\langle v^+ \rangle_{EP}$ are observed at both sides of the central high negative $\langle v^+ \rangle_{EP}$ in Fig. 13(d). This alternating pattern can be interpreted as being symptomatic of sweep and ejection behaviors induced by a strong quasi-streamwise vortex; that is, the reduced streamwise momentum at the upwash flank of the vortex is the result of the low-speed flow ejected from the inner layer, whereas the enhanced streamwise momentum at the downwash flank of the vortex is caused by the high-speed flow transported from the outer layer. However, we remark that even though $\langle u^+ \rangle_{EP}$ (not shown) and $\langle v^+ \rangle_{EP}$ [see Figs. 14(c) and 14(d)] around an EP event of q' exhibit a qualitatively similar behavior, providing evidence for the significance of the Q4 event in the buffer region, the flow dynamics related to the

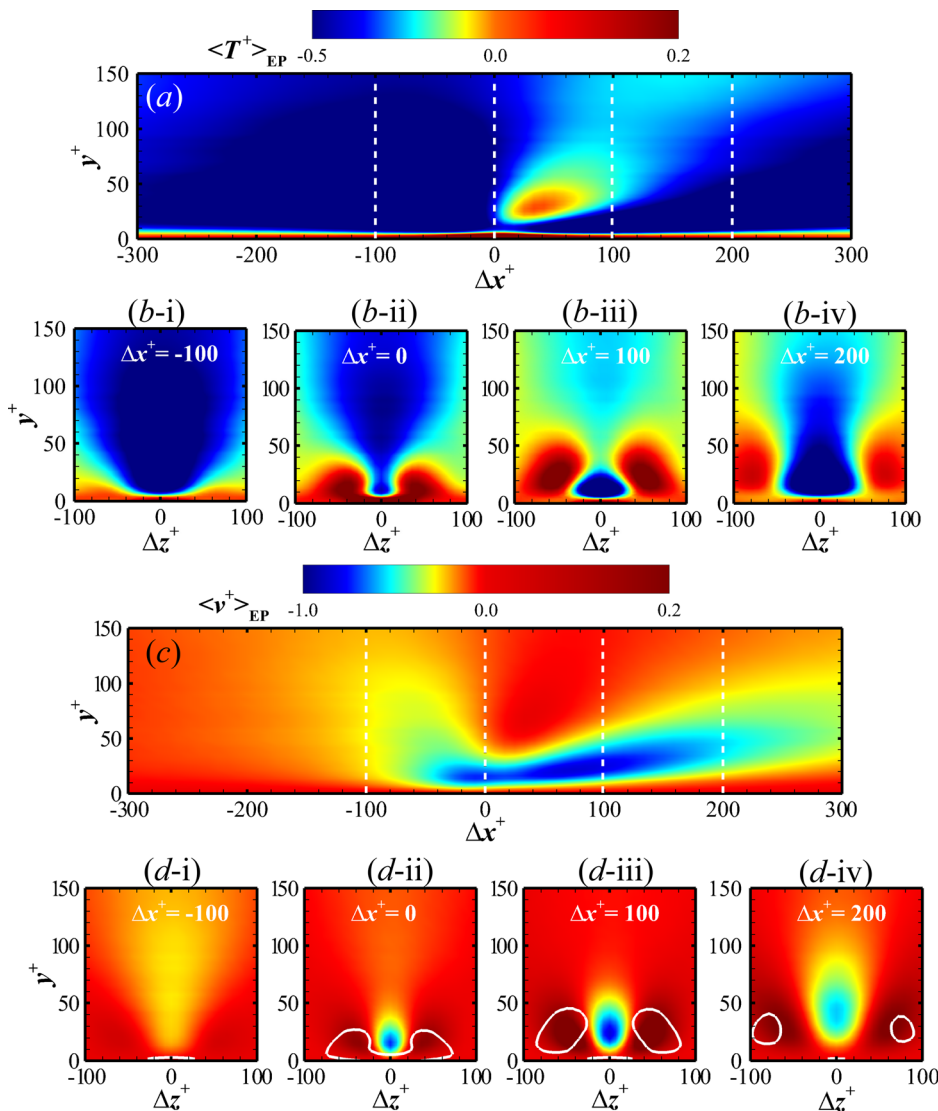


FIG. 14. Conditionally averaged temperature and velocity fluctuations associated with an EP event of q' at $\Delta x^+ = 0$ and $\Delta z^+ = 0$. (a) and (c) Temperature and wall-normal velocity in the $(\Delta x^+, y^+)$ plane at $\Delta z^+ = 0$. (b) and (d) Temperature and wall-normal velocity in the $(\Delta z^+, y^+)$ plane at four streamwise locations marked by dashed lines in (a) and (c). White solid lines in (d) denote $\langle T^+ \rangle_{EP} = 0.08$.

EP q' events are not the same. Looking at $\langle T^+ \rangle_{EP}$ in Fig. 14(a), there exists a characteristic two-layer structure, whereby positive temperature fluctuations are located in the inner layer very close to the wall, and negative temperature fluctuations are distributed in most of the boundary layer. This trend of $\langle T^+ \rangle_{EP}$ is directly related to the existence of an inflection point in the mean temperature profile due to wall cooling, contrary to the monotonic changes in the mean streamwise velocity profile. Further, an inspection of the $(\Delta z^+, y^+)$ planes of $\langle T^+ \rangle_{EP}$ displayed in Fig. 14(b) proves that the EP events of q' are related to the highly squeezed high-temperature flow in the inner layer $y^+ < 10$. Clearly, the upper low-temperature flow coming from the outer region squeezes down the high-temperature flow covering the wall, which rolls up two high-temperature regions along the spanwise direction. It can be seen that the severely squeezed high-temperature flow is not penetrated, still showing coherence, and no low-temperature flow arrives at the wall. Thus, it is reasonable to infer that the downward extrusion motion of the low-temperature flow is unlike the aforementioned downwash motion of the high-speed flow induced by a strong streamwise vortex, as previously discussed with regard to Fig. 13.

Figures 15(a) and 15(b) show enlarged views of $\langle u^+ \rangle_{EP}$ and $\langle T^+ \rangle_{EP}$, respectively, in the transverse section at $\Delta x^+ = 0$, together with streamlines and vector plots, and these help elucidate the differences between the conditionally averaged fields around EP events of τ' and q' . Both figures reveal a similar qualitative flow pattern for $y^+ > 50$, with a pair of large-scale counter-rotating vortices transporting the outer high-momentum flow or the outer low-temperature flow toward the overlap region, consistent with the observation by Guerrero *et al.*²² The greatest difference between two figures lies in the near-wall region.

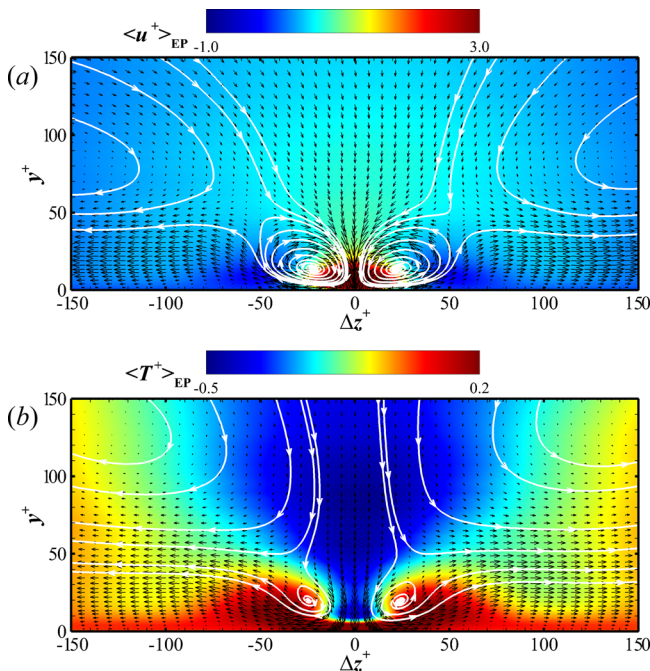


FIG. 15. Enlarged views of conditionally averaged fluctuations with overlapped white streamlines in the $(\Delta z^+, y^+)$ plane at $\Delta x^+ = 0$: (a) $\langle u^+ \rangle_{EP}$; (b) $\langle T^+ \rangle_{EP}$. Black arrows denote velocity vectors in the plane.

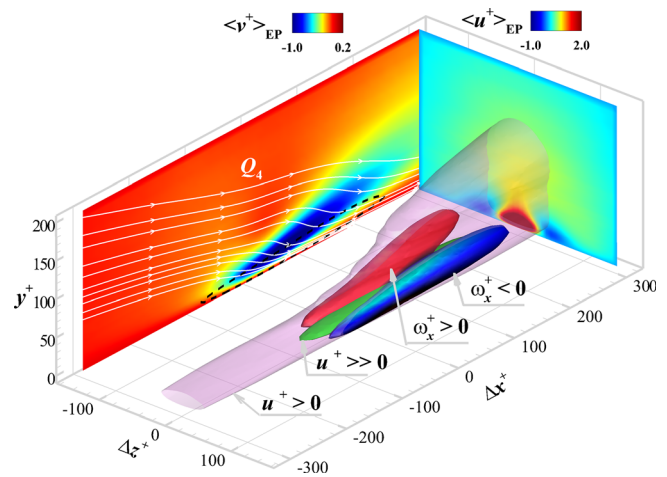


FIG. 16. Conditionally averaged three-dimensional fluctuating fields associated with an EP event of τ' at $\Delta x^+ = 0$ and $\Delta z^+ = 0$. The pink isosurface is $u^+ = 0.8$, and the green isosurface and black dashed line, are $u^+ = 2.5$. Red and blue isosurfaces, flanking the central high-speed streak, represent the two quasi-streamwise vortices displayed by the Q criterion ($Q/Q_{max} = 5\%$) and colored by the streamwise vorticity $\omega_x^+ > 0$ and $\omega_x^+ < 0$, respectively. Conditional averages in two sliced planes at $\Delta z^+ = 0$ and $\Delta x^+ = 0$ are shifted for better visualization.

In Fig. 15(a), a pair of small-scale counter-rotating vortices with a spanwise extension of approximately 100 wall units is induced by the outer vortices and emerges just above the EP event. Between the two induced vortices close to the wall, the sweep motion of the transported high-velocity flow located on both downwash sides causes an EP event of τ' , whereas the ejection of the low-velocity flow occurs on the upwash sides of both vortices, in accordance with the conditional

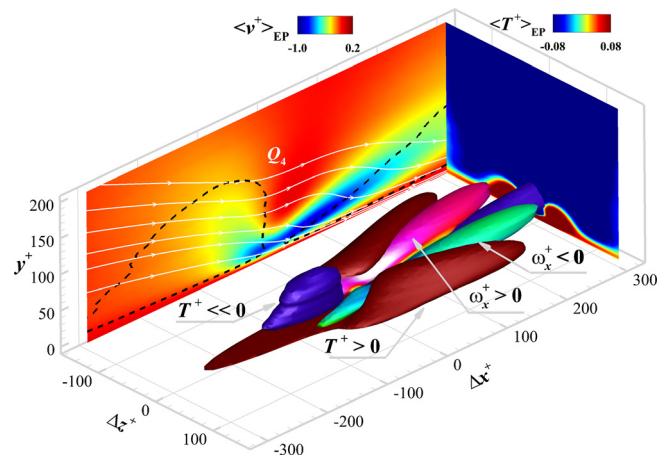


FIG. 17. Conditionally averaged three-dimensional fluctuating fields associated with an EP event of q' at $\Delta x^+ = 0$ and $\Delta z^+ = 0$. The purple isosurface is $T^+ = -0.7$, the red isosurface is $T^+ = 0.08$, and the black dashed line is $T^+ = -0.5$. Pink and green isosurfaces, being wrapped by the high-temperature flow, represent the two quasi-streamwise vortices displayed by the Q criterion ($Q/Q_{max} = 5\%$) and colored by the streamwise vorticity $\omega_x^+ > 0$ and $\omega_x^+ < 0$, respectively. Conditional averages in two sliced planes at $\Delta z^+ = 0$ and $\Delta x^+ = 0$ are shifted for better visualization.

coherent structures studied by Guerrero *et al.*²² In contrast to this, no distinct vortical structures are observed in the near-wall region of $\langle T^+ \rangle_{EP}$, except for a pair of very small counter-rotating vortices in the interface region between the high- and low-temperature flows. As shown in Fig. 15(b), both small vortices are generated mainly by the combined action of the downward extrusion motion of the low-temperature flow and the upward rolling motion of the high-temperature flow, exhibiting no substantial effect on the EP event. Interestingly, the EP event of q' is a product of the extrusion motion of the upper low-temperature flow, which can be vividly interpreted as a fist hitting the high-temperature flow on the wall (see the low-temperature flow in the region $-20 < \Delta x^+ < 20$ and $10 < y^+ < 30$).

To describe the overall organization of the coherent structures responsible for the EP event, three-dimensional views of the conditionally averaged fields are given in Figs. 16 and 17 for an EP event of τ' and an EP event of q' , respectively, where isosurfaces of the streamwise velocity fluctuation $\langle u^+ \rangle_{EP}$ and temperature fluctuation $\langle T^+ \rangle_{EP}$

are shown, as well as an isosurface of the second invariant of the velocity gradient Q , normalized by its maximum value Q_{max} . Two slices are also included for better explanation: one at $\Delta x^+ = 0$ and another at $\Delta z^+ = 0$. In both figures, the quasi-streamwise vortices are made visible by the isosurface of $Q/Q_{max} = 0.05$ and colored by the streamwise vorticity, ω_x^+ .

Looking at the conditional field of $\langle u^+ \rangle_{EP}$ in Fig. 16, a region of high streamwise velocity fluctuation related to the EP event, made visible by the green isosurface of $\langle u^+ \rangle_{EP} = 2.5$, is seen between the energetic clockwise and counterclockwise quasi-streamwise vortices, which are represented by the red ($\omega_x^+ > 0$) and blue ($\omega_x^+ < 0$) isosurfaces, respectively. This flow topology also confirms what was indicated by the above two-dimensional representations, namely, that the EP event of the WSS fluctuations is strongly associated with the quasi-streamwise vortices. The quasi-streamwise vortices become larger and higher downstream of the EP event, eventually leading to an upward-lifting movement of the high-velocity structure, which is better seen in

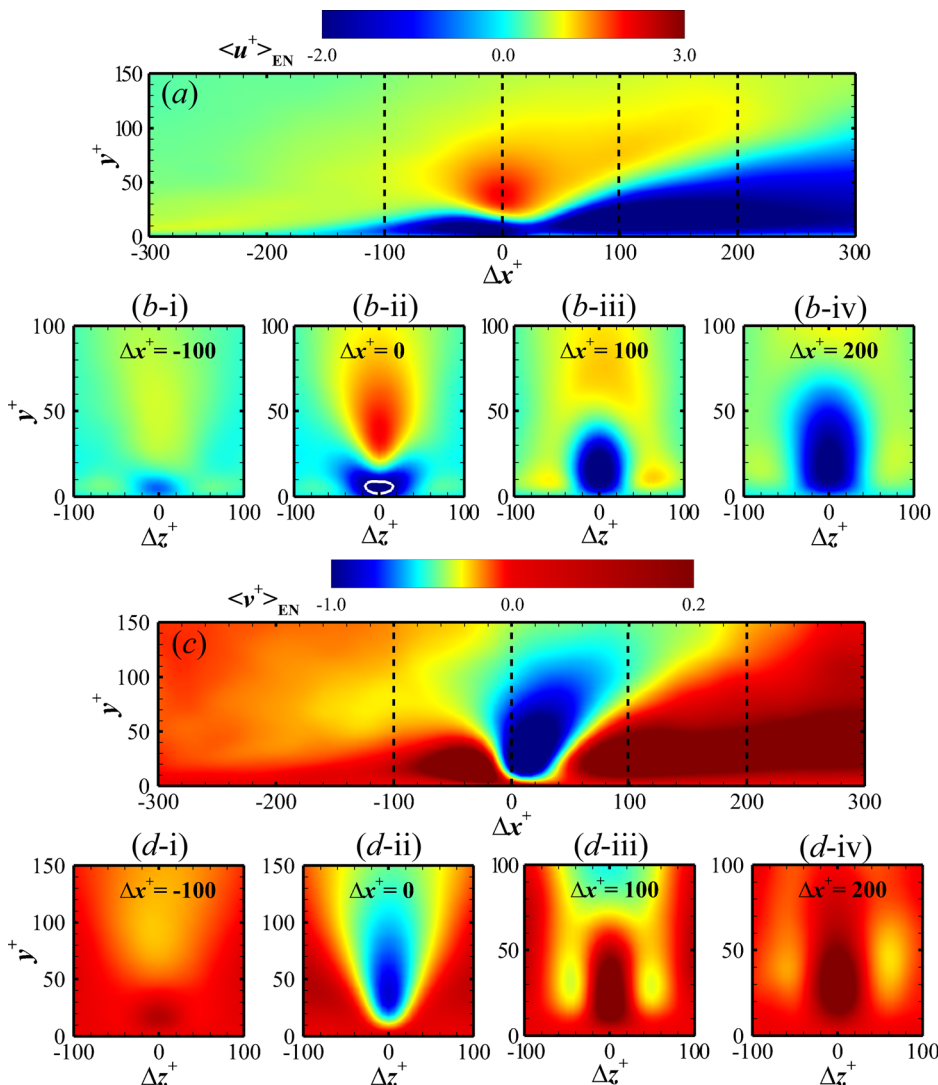


FIG. 18. Conditionally averaged velocity fluctuations associated with an EN event of τ' at $\Delta x^+ = 0$ and $\Delta z^+ = 0$. (a) and (c) Streamwise and wall-normal velocities in the $(\Delta x^+, y^+)$ plane at $\Delta z^+ = 0$. (b) and (d) Streamwise and wall-normal velocities in the $(\Delta z^+, y^+)$ plane at four streamwise locations marked by dashed lines in (a) and (c). The white solid lines in (b) and (d) denote $\langle u^+ \rangle_{EN} = -2.0$.

Fig. 13(b). In addition, the main coherent structures are surrounded by a large-scale inclined region of positive fluctuation $\langle u^+ \rangle_{EP} = 0.8$, represented by the pink isosurface, which has a characteristic length of 300 wall units and extends up to $y^+ \approx 150$. This large-scale velocity structure is a signature of the outer counter-rotating motions, as observed in Fig. 15, and it has previously been observed in conditionally averaged volumetric flow fields by Guerrero *et al.*²² However, it should be emphasized that Guerrero *et al.*²² used a two-step conditional average, considering the vortex location with respect to the flow direction, and performed the conditional analysis based on a left-side or a right-side vortex. Finally, the slice at $\Delta z^+ = 0$ is shifted to the left of the box, and the displayed streamwise lines indicate a strong Q4 event above and downstream of the EP event, characterized by high positive $\langle u^+ \rangle_{EP}$ and negative $\langle v^+ \rangle_{EP}$.

The conditional three-dimensional field of $\langle T^+ \rangle_{EP}$ reported in Fig. 17 exhibits a different scenario. As expected, the high-temperature

flow around an EP event of q' , made visible by the dark red isosurface of $\langle T^+ \rangle_{EP} = 0.08$, which is highly squeezed by the low-temperature flow represented by the purple isosurface of $\langle T^+ \rangle_{EP} = -0.7$, is also associated with a strong Q4 event (see the white streamlines in the slice at $\Delta z^+ = 0$). It is interesting to note that the high-temperature flow on the wall still retains coherence, whereas the downward extrusion does not break it but rolls up the fluids on both spanwise sides. As a result, the upper low-temperature flow cannot reach the wall, and the upward rolling motion induces a pair of quasi-streamwise vortices downstream, represented by the pink and green isosurfaces, respectively, both of which are located above the high-temperature flow. Therefore, it is believed that the EP event of q' is mainly linked to the downward extrusion of the upper low-temperature flow, and the high-temperature flow plays a relatively passive role in EP event generation.

Next, we analyze the conditionally averaged fluctuation fields around an EN event, as presented in Figs. 18 and 19 for τ' and q' ,

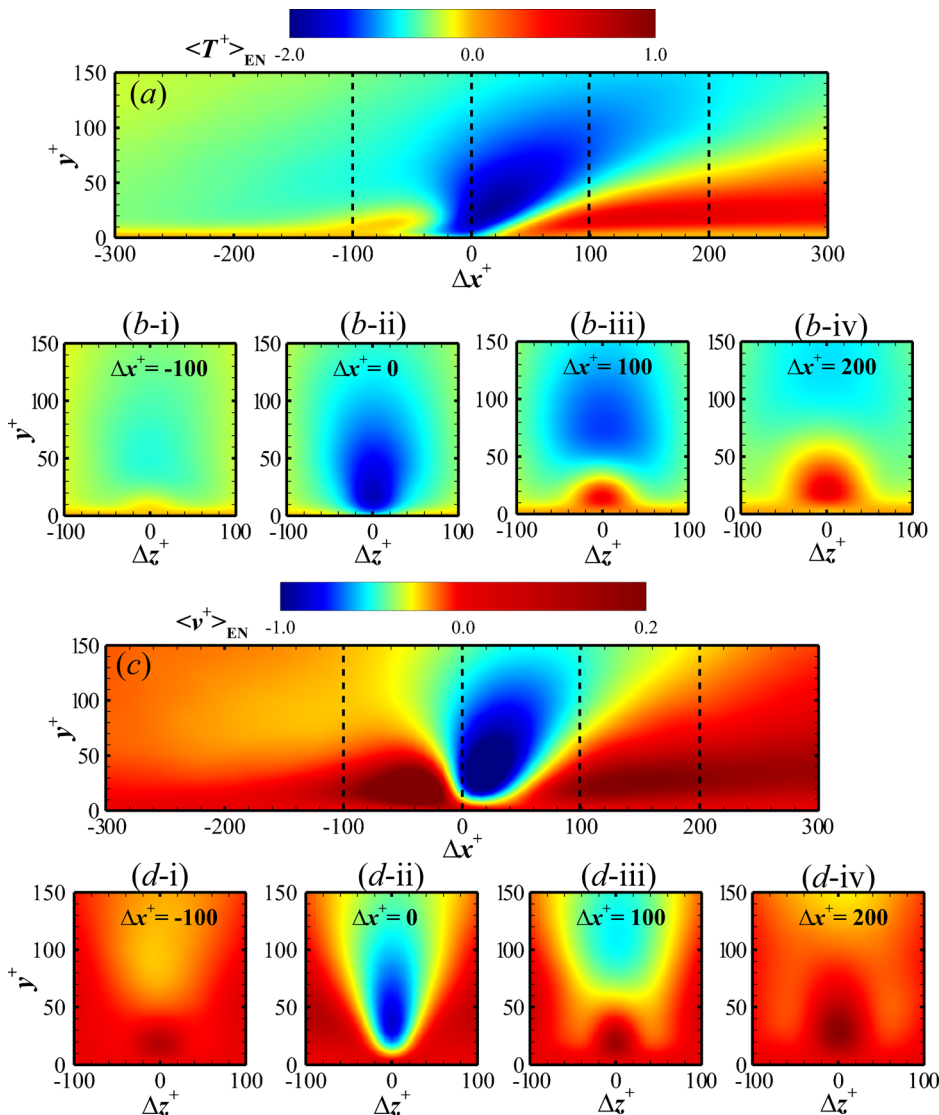


FIG. 19. Conditionally averaged temperature velocity fluctuations associated with an EN event of q' at $\Delta x^+ = 0$ and $\Delta z^+ = 0$. (a) and (c) Temperature and wall-normal velocities in the $(\Delta x^+, y^+)$ plane at $\Delta z^+ = 0$. (b) and (d) Temperature and wall-normal velocities in the $(\Delta z^+, y^+)$ plane at four streamwise locations marked by dashed lines in (a) and (c).

respectively. Figures 18(a), 18(c), 19(a), and 19(c) show the conditionally averaged fields in the $(\Delta x^+, y^+)$ plane at $\Delta z^+ = 0$, while Figs. 18(b), 18(d), 19(b), and 19(d) show the fluctuations in the $(\Delta z^+, y^+)$ plane at $\Delta x^+ = -100, 0, 100$, and 200. As can be seen in Fig. 18(a), $\langle u^+ \rangle_{EP}$ indicates that the EN event of τ' is associated with an inclined large-scale low-speed region, which bellows a large scale of the positive velocity fluctuations in the buffer and outer regions. This flow pattern is in good agreement with the conditional average above a critical point at the wall obtained by Chin *et al.*⁵⁹ and the averaged velocity fluctuations related to the backflow event obtained by Guerrero *et al.*²² Regarding the wall-normal velocity fluctuation in Fig. 19(c), there exists a region of large negative $\langle v^+ \rangle_{EP}$ above and downstream of the extreme event, extending up to $y^+ = 150$. Careful examinations of the large positive $\langle u^+ \rangle_{EP}$ and large negative $\langle v^+ \rangle_{EP}$ for $y^+ > 10$ in the transverse temperature section at $\Delta x^+ = 0$, shown in Figs. 18(b) and 18(d), respectively, reveal that the EN event of τ' is likely to be produced by strong compression of the low-speed structure on the wall by the upper high-speed structure.

In Fig. 19(a), $\langle T^+ \rangle_{EN}$ suggests a different mechanism, namely, destruction of the high-temperature structure on the wall by an inclined large-scale low-temperature structure, which originates from the wall in the range $-10 < \Delta x^+ < 10$ and becomes larger as it moves higher. Looking at the wall-normal velocity field shown in Fig. 19(c), it should be noted that this upper low-temperature structure is accompanied by a large region of negative $\langle v^+ \rangle_{EN}$. Since the large-scale low-temperature structure directly impinges on the wall with large speed, the main reason for the EN event of q' becomes apparent, which can be better seen from the temperature and wall-normal velocity in the $(\Delta z^+, y^+)$ plane at $\Delta x^+ = 0$, as displayed in Figs. 19(b) and 19(d). Another important aspect of the conditional fields for q' is the coherent structure of the positive and negative $\langle v^+ \rangle_{EN}$ in the $(\Delta x^+, y^+)$ and $(\Delta z^+, y^+)$ planes, very similar to the wall-normal velocity fluctuations shown in Figs. 18(c) and 18(d) for τ' . Such behavior is associated with a strong oblique vortex, as suggested by Guerrero *et al.*²² and Lenaers *et al.*⁶⁰ in backflow conditioned flow fields. More evidence of the strong oblique vortex will be provided by the conditioned three-dimensional flow fields.

Figures 20(a) and 20(b) show enlarged views of $\langle u^+ \rangle_{EN}$ and $\langle T^+ \rangle_{EN}$, respectively, together with vector plots in the $(\Delta x^+, y^+)$ plane at $\Delta z^+ = 0$. They highlight that positive $\langle u^+ \rangle_{EN}$ and negative $\langle T^+ \rangle_{EN}$ are related to a strong Q4 event, which is transported from the logarithmic region toward the wall by the sweep motion, whereas negative $\langle u^+ \rangle_{EN}$ and positive $\langle T^+ \rangle_{EN}$ are associated with a Q2 event, which is ejected from the wall to the overlap region and the logarithmic region. The vector plots show that there exist two converging Q4/Q2 pairs inclined downstream, with a strong clockwise-rotating spanwise vortex in the middle. Specifically, a small Q2 (ejection) region close to the wall appears upstream of the EN event at $\Delta x^+ < -40$, followed by another large Q2 (ejection) region downstream at $\Delta x^+ > 100$. Accordingly, the Q4 (sweep) region is clearly visible in the upper left part of both figures, implying a strong top-down interaction between the near-wall and outer regions. Such a converging Q4/Q2 pattern is similar to the hairpin vortex signatures proposed by Lee and Sung⁶¹ and Adrian *et al.*⁵² in streamwise/wall-normal cuts through a hairpin vortex center. Note that the small spanwise vortex is only a Δx^+-y^+ cut through the aforementioned strong oblique vortex, but the remarkable effect of the downward motions of this vortex on the high-speed and low-temperature fluids is still clearly observed.

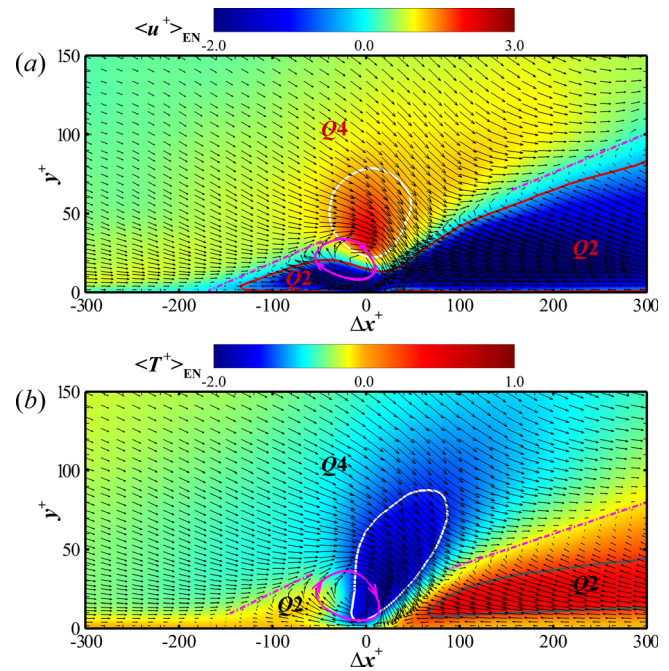


FIG. 20. Enlarged view of conditionally averaged fluctuations with overlapped velocity vectors in the $(\Delta x^+, y^+)$ plane at $\Delta z^+ = 0$: (a) $\langle u^+ \rangle_{EN}$; (b) $\langle T^+ \rangle_{EN}$. The red line in (a) denotes $\langle u^+ \rangle_{EN} = -0.3$ and the black line in (b) denotes $\langle T^+ \rangle_{EN} = 0.3$. The white solid lines denote $\langle u^+ \rangle_{EN} = 1.3$ in (a) and $\langle T^+ \rangle_{EN} = -1.3$ in (b). The inclined shear layers associated with the Q2 and Q4 events are indicated schematically by the dashed pink lines. The pink solid line depicts the clockwise rotating vortex.

The conditioned three-dimensional coherent structures associated with EN events of τ' and q' at $\Delta x^+ = 0$ and $\Delta z^+ = 0$ are shown in Figs. 21 and 22, respectively. Both figures confirm the existence of a pair of counter-rotating oblique vortices, which are visualized by the isosurface of $Q/Q_{max} = 0.05$ and colored by the streamwise vorticity ω_x^+ . Here, the left-side clockwise vortex and the right-side counter-clockwise oblique vortex are marked as Q_L and Q_R , respectively. It can be seen that these two attached oblique vortices become larger and get lifted up downstream of the extreme wall event. In Fig. 21, a large-scale elongated region of negative fluctuation in the middle of the oblique vortex pair forms a low-speed streak, made visible by the blue isosurface of $\langle u^+ \rangle_{EN} = -0.3$. Consistent with the backflow conditional average of Guerrero *et al.*²² this low-speed streak is also characterized by a spanwise meandering behavior owing to the oblique vortices at $\Delta x^+ \approx 0$, which is better seen in the figure insert, which shows the top view of the conditioned structures. In addition, a small ellipsoidal region of positive velocity fluctuation, indicated by the red isosurface of $\langle u^+ \rangle_{EN} = -1.3$ (a very large value chosen to highlight the high-momentum structure), is clearly found just above and between the two oblique vortices, where the induced downwash motion is predominant, as observed in Fig. 20(a). Furthermore, a qualitatively similar flow topology is also observed in Fig. 22. As can be seen, an inclined large-scale region of low-temperature structure, indicated by the blue isosurface of $\langle T^+ \rangle_{EN} = -1.1$, appears between the upper parts of the two oblique vortices, and an elongated high-temperature streak, made

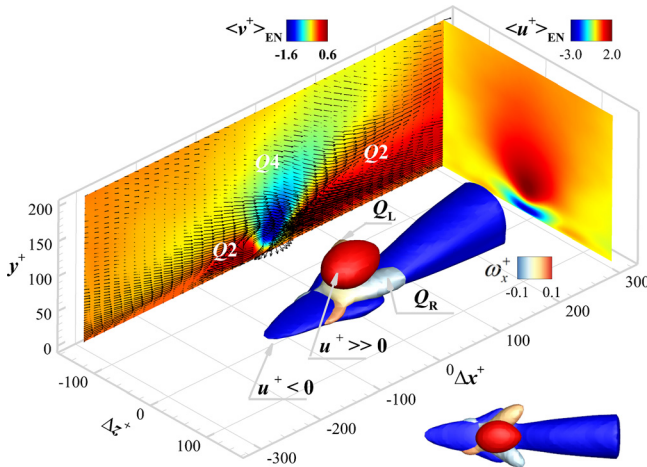


FIG. 21. Conditionally averaged three-dimensional fluctuating fields associated with an EN event of τ^+ at $\Delta x^+ = 0$ and $\Delta z^+ = 0$. The red isosurface is $\langle u^+ \rangle_{EN} = 1.3$, and the blue isosurface is $\langle u^+ \rangle_{EN} = -0.3$. The two oblique vortices marked as the left-side vortex (Q_L) and the right-side vortex (Q_R) are displayed by the Q criterion ($Q/Q_{max} = 5\%$) and colored by the streamwise vorticity ω_x^+ . The conditional averages in two sliced planes at $\Delta z^+ = 0$ and $\Delta x^+ = 0$ are shifted for better visualization.

visible by the red isosurface of $\langle T^+ \rangle_{EN} = 0.08$, expands downstream of the EN event. It is clear that the high-temperature streak does not exhibit meandering behavior. This is probably due to the significant impact of the large-scale low-temperature structure driven by the downwash motion of the oblique vortices, which destroys the structural coherence, as suggested by a comparison of Fig. 20(b) with Fig. 20(a). Overall, these findings support the previous numerical and

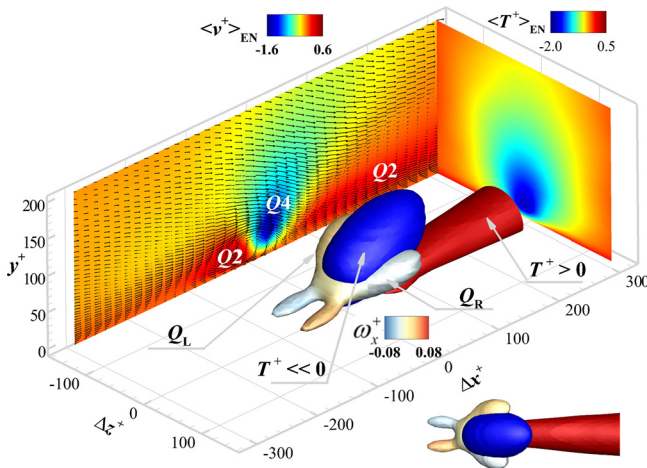


FIG. 22. Conditionally averaged three-dimensional fluctuating fields associated with an EN event of q^+ at $\Delta x^+ = 0$ and $\Delta z^+ = 0$. The red isosurface is $\langle T^+ \rangle_{EN} = 0.08$, and the blue isosurface is $\langle T^+ \rangle_{EN} = -1.1$. The two oblique vortices marked as the left-side vortex (Q_L) and the right-side vortex (Q_R) are displayed by the Q criterion ($Q/Q_{max} = 5\%$) and colored by the streamwise vorticity ω_x^+ . The conditional averages in two sliced planes at $\Delta z^+ = 0$ and $\Delta x^+ = 0$ are shifted for better visualization.

experimental studies conducted by Cardesa *et al.*⁶³ in turbulent channel flow and by Bross *et al.*⁶⁴ in an adverse pressure gradient TBL, which revealed that the backflow event was generated under a low-momentum region and was related to oblique vortices located at the buffer, and further demonstrate the essential role of the strong oblique vortex in the generation of the EN WHF event.

C. Decomposition of mean shear stress and heat flux

Performing a scale-based decomposition analysis of the mean wall skin friction coefficient C_f and the wall heat transfer coefficient C_h through the RD identity^{28–30} can provide useful information for quantifying the contribution of the associated coherent turbulent structure with a specific length scale to the mean shear stress and heat flux generation at the wall. These coefficients are defined as

$$C_f = \frac{2\overline{\tau(x, z, t)}}{\rho_\infty U_\infty^2} \quad \text{and} \quad C_h = \frac{\overline{q(x, z, t)}}{\rho_\infty U_\infty^3}. \tag{7}$$

Following Li *et al.*²⁹ and Fan *et al.*,³⁰ the decomposition of C_f for a compressible zero-pressure-gradient flat-plate TBL is cast in the form

$$C_f = C_{f,V} + C_{f,T} + C_{f,G}, \tag{8}$$

where $C_{f,V}$, $C_{f,T}$, and $C_{f,G}$, respectively, denote the contributions of direct viscous dissipation, the power spent in turbulence kinetic energy (TKE) production, and the streamwise heterogeneity. The three terms can be explicitly expressed as follows:

$$\begin{aligned} C_{f,V} &= \frac{2}{\rho_\infty U_\infty^3} \int_0^\infty \bar{\tau}_{yx} \frac{\partial \tilde{u}}{\partial y} dy, \\ C_{f,T} &= \frac{2}{\rho_\infty U_\infty^3} \int_0^\infty \bar{\rho} (-\tilde{u}'' \tilde{v}'') \frac{\partial \tilde{u}}{\partial y} dy, \\ C_{f,G} &= \underbrace{\frac{2}{\rho_\infty U_\infty^3} \int_0^\infty (\tilde{u} - U_\infty) \bar{\rho} \left(\tilde{u} \frac{\partial \tilde{u}}{\partial x} + \tilde{v} \frac{\partial \tilde{u}}{\partial y} \right) dy}_{C_{f,G1}} \\ &\quad + \underbrace{\frac{2}{\rho_\infty U_\infty^3} \int_0^\infty (\tilde{u} - U_\infty) \frac{\partial}{\partial x} (\bar{\rho} \tilde{u}'' \tilde{u}'' - \bar{\tau}_{xx}) dy}_{C_{f,G2}} \\ &\quad + \underbrace{\frac{2}{\rho_\infty U_\infty^3} \int_0^\infty (\tilde{u} - U_\infty) \frac{\partial \bar{P}}{\partial x} dy}_{C_{f,G3}}. \end{aligned} \tag{9}$$

Likewise, similar to the decomposition formula proposed by Sun *et al.*³⁴ through an integration of the compressible total energy equation from the wall to the free stream, the mean wall heat transfer coefficient C_h is decomposed as

$$C_h = C_{h,C} + C_{h,TH} + C_{h,MD} + C_{h,TKE} + C_{h,MS} + C_{h,RS} + C_{h,G}, \tag{10}$$

where

$$\begin{aligned} C_{h,C} &= \frac{1}{\rho_\infty U_\infty^4} \int_0^\infty k \frac{\partial \bar{T}}{\partial y} \frac{\partial \tilde{u}}{\partial y} dy, \\ C_{h,TH} &= \frac{1}{\rho_\infty U_\infty^4} \int_0^\infty -c_p \bar{\rho} \tilde{v}'' \tilde{T}'' \frac{\partial \tilde{u}}{\partial y} dy, \end{aligned} \tag{11}$$

$$\begin{aligned}
 C_{h,MD} &= \frac{1}{\rho_\infty U_\infty^4} \int_0^\infty \overline{u''_k \sigma_{kj}} \frac{\partial \tilde{u}}{\partial y} dy, \\
 C_{h,TKE} &= \frac{1}{\rho_\infty U_\infty^4} \int_0^\infty -\frac{1}{2} \overline{\rho u''_k u''_l u''_k u''_l} \frac{\partial \tilde{u}}{\partial y} dy, \\
 C_{h,MS} &= \frac{1}{\rho_\infty U_\infty^4} \int_0^\infty \tilde{u}_k \overline{\sigma_{kj}} \frac{\partial \tilde{u}}{\partial y} dy, \\
 C_{h,RS} &= \frac{1}{\rho_\infty U_\infty^4} \int_0^\infty -\tilde{u}_k \overline{\rho u''_k u''_l} \frac{\partial \tilde{u}}{\partial y} dy, \\
 C_{h,G} &= \frac{1}{\rho_\infty U_\infty^4} \int_0^\infty (\tilde{u} - U_\infty) \left[\bar{\rho} \frac{D\tilde{E}}{Dt} + \frac{\partial(\tilde{u}\bar{p})}{\partial x} + \frac{\partial(\tilde{v}\bar{p})}{\partial y} \right. \\
 &\quad \left. - \left(k \frac{\partial \tilde{T}}{\partial x} - c_p \bar{\rho} \overline{u''_k T''} + \overline{u''_k \sigma_{ki}} - \frac{1}{2} \overline{\rho u''_k u''_l u''_k u''_l} \right. \right. \\
 &\quad \left. \left. + \tilde{u}_k \overline{\sigma_{kj}} - \tilde{u}_k \overline{\rho u''_k u''_l} \right) \right] dy
 \end{aligned}$$

The term $C_{h,C}$ is associated with heat conduction, $C_{h,TH}$ is associated with turbulent transport of heat, involving the wall-normal heat flux, $C_{h,MD}$ is the wall-normal component of the molecular diffusion, $C_{h,TKE}$ is turbulent transport of TKE, $C_{h,MS}$ and $C_{h,RS}$ are associated with the molecular stresses and the Reynolds stresses, respectively, and $C_{h,G}$ is associated with the variation of the specific total energy E with time, the pressure, and the streamwise heterogeneity. Here, τ_{xx} and τ_{yx} denote the streamwise components of the shear and normal stress, respectively, and σ_{ij} denotes the viscous stress.

The full compositions of C_f and C_h are quantitatively compared in Fig. 23. The reliability of the decomposition methods is confirmed by computing the relative errors, defined as $(C_{f,V} + C_{f,T} + C_{f,G} - C_{f,DNS})/C_{f,DNS}$ and $(C_{h,C} + C_{h,TH} + C_{h,MD} + C_{h,TKE} + C_{h,MS} + C_{h,RS} + C_{h,G} - C_{h,DNS})/C_{h,DNS}$, respectively, where $C_{f,DNS}$ and $C_{h,DNS}$ are directly calculated using Eq. (7). As can be seen, the relative errors are estimated to 0.00% for C_f and $-1.03%$ for C_h , indicating that the accuracy of the decompositions is very satisfactory. For C_f as shown in Fig. 23(a), $C_{f,V}$ and $C_{f,T}$ are predominant, attaining approximately 41.73% and 45.02% of the total skin friction, respectively, while the contribution of $C_{f,G}$ is rather small, about 13.25% and comes mostly from the convection term $C_{f,G1}$. This trend is consistent with the DNS

study of a supersonic boundary layer at Mach 2 for $Re_\tau = 250-1110$ by Fan *et al.*,³⁰ who found that $C_{f,V}$ and $C_{f,T}$ yield up to 90% of the total C_f . With regard to C_h , a different behavior is observed in Fig. 23(b). Positive $C_{h,RS}$ takes the leading role, even larger than the total wall heat transfer, reaching approximately 126.67%, and counteracts the large negative contribution of $C_{h,TH}$, which is about $-76.64%$. For comparison, the heat transfer decomposition of a hypersonic boundary layer at Mach 6 and $Re_\infty/\text{mm} = 12000$ conducted by Sun *et al.*³⁴ had values of 120% and $-71.3%$ for $C_{h,RS}$ and $C_{h,TH}$, respectively. In addition, another large component $C_{h,MS}$ contributes positively to 44.21% of C_h , whereas the positive contributions of $C_{h,G}$ and $C_{h,MD}$, as well as the negative contributions of $C_{h,C}$ and $C_{h,TKE}$ can be neglected, owing to their rather small magnitudes. This phenomenon can be better understood as the excessive heat at the wall generated by the work of the Reynolds stresses $C_{h,RS}$ and the molecular stresses $C_{h,MS}$ being carried away from the wall toward the outer region through the turbulent transport $C_{h,TH}$.

To further reveal the quantitative contribution of the turbulent coherent structures to C_f and C_h , we focus on the $C_{f,T}$ contribution and the $C_{h,RS}$ and $C_{h,TH}$ contributions. Following Fan *et al.*,³³ the streamwise and wall-normal velocity fluctuations, as well as the temperature fluctuations, are all decomposed into four different terms with specific spanwise length scales by applying a bi-dimensional empirical mode decomposition (BEMD),^{35,65} given by

$$\begin{aligned}
 u'' &= u''_1 + u''_2 + u''_3 + u''_4, \\
 v'' &= v''_1 + v''_2 + v''_3 + v''_4, \\
 T'' &= T''_1 + T''_2 + T''_3 + T''_4,
 \end{aligned} \tag{12}$$

where the subscripts 1, 2, 3, and 4 stand for the fluctuations with increasing spanwise length scales, corresponding to the four modes of BEMD. Therefore, the Reynolds shear stress in Eqs. (9) and (11) can be decomposed into four diagonal terms and 12 nondiagonal terms and rewritten as

$$-\overline{u''v''} = -\sum_{i=1}^4 \overline{u''_i v''_i} - \sum_{i=1, j=1, i \neq j}^4 \overline{u''_i v''_j}. \tag{13}$$

Similarly, the wall-normal heat flux in Eq. (11) can be rewritten as

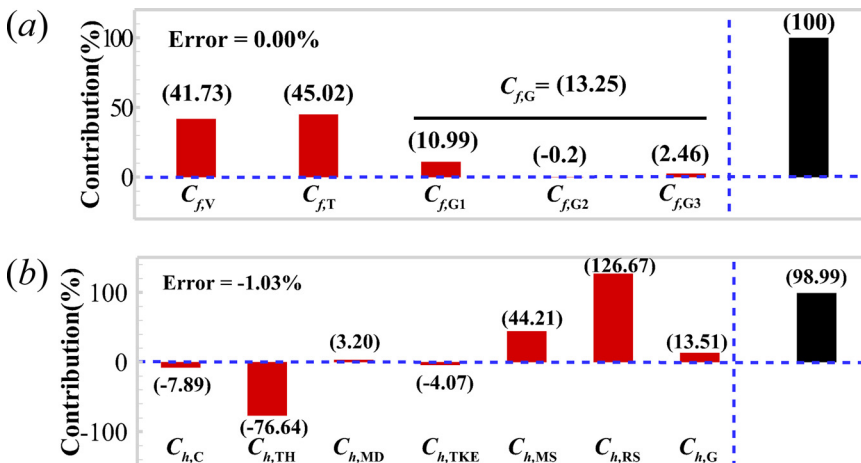


FIG. 23. Contributions of the decomposed components: (a) C_f ; (b) C_h . Black bars denote the sums of the decomposed components.

$$-\widetilde{v''T''} = -\sum_{i=1}^4 \widetilde{v''_i T''_i} - \sum_{i=1, j=1, i \neq j}^4 \widetilde{v''_i T''_j}. \quad (14)$$

As a result, the $C_{f,T}$ contribution in Eq. (9) and the $C_{h,RS}$ and $C_{h,TH}$ contributions in Eq. (11) can also be divided into 16 terms, given by

$$\begin{aligned} C_{f,T} &= \underbrace{\frac{2}{\rho_\infty U_\infty^3} \int_0^\infty \bar{\rho} (-u''_1 v''_1) \frac{\partial \widetilde{u}}{\partial y} dy + \dots}_{(1,1)} \\ &\quad + \underbrace{\frac{2}{\rho_\infty U_\infty^3} \int_0^\infty \bar{\rho} (-u''_4 v''_4) \frac{\partial \widetilde{u}}{\partial y} dy,}_{(4,4)} \\ C_{h,RS} &= \underbrace{\frac{1}{\rho_\infty U_\infty^4} \int_0^\infty -\widetilde{u} \bar{\rho} u''_1 v''_1 \frac{\partial \widetilde{u}}{\partial y} dy + \dots}_{(1,1)} \\ &\quad + \underbrace{\frac{1}{\rho_\infty U_\infty^4} \int_0^\infty -\widetilde{u} \bar{\rho} u''_4 v''_4 \frac{\partial \widetilde{u}}{\partial y} dy,}_{(4,4)} \\ C_{h,TH} &= \underbrace{\frac{1}{\rho_\infty U_\infty^4} \int_0^\infty -c_p \bar{\rho} v''_1 T''_1 \frac{\partial \widetilde{u}}{\partial y} dy + \dots}_{(1,1)} \\ &\quad + \underbrace{\frac{1}{\rho_\infty U_\infty^4} \int_0^\infty -c_p \bar{\rho} v''_4 T''_4 \frac{\partial \widetilde{u}}{\partial y} dy.}_{(4,4)} \end{aligned} \quad (15)$$

Each component is labeled by a mode number index (i, j) , where i and j denote the i th and j th modes of the BEMD. Considering that the spanwise length scale λ_z of a BEMD mode is increased as the mode number increases, the four diagonal components represent the contributions associated with specific spanwise length scales. Specifically, the components (1, 1) and (4, 4) denote the contributions of small- and large-scale structures, respectively, whereas the components (2, 2) and (3, 3) are related to intermediate-scale structures. The other 12

nondiagonal components represent the contributions generated by interactions between structures with different spanwise length scales, as suggested by Cheng *et al.*³⁵ for turbulent channel flows.

Figure 24 shows the premultiplied spanwise spectra of u'' , v'' , and T'' in the first mode, together with the full spectra calculated from the original DNS data. Note that the original spectra of u'' , v'' , and T'' are characterized by an inner peak with a spanwise length scale of the magnitude of 100 wall units, and no energy peak is evident in the outer region, owing to the low Reynolds number considered in the present study. As expected, the decomposed fluctuations are primarily confined in the small- (y^+, λ_z^+) domain, compared with the original spectra (indicated by the solid black isolines). For u'' , the spectra in Fig. 24(a) peak at $y^+ = 12$ and $\lambda_z^+ = 81$, smaller than the primary inner peak appearing at $y^+ = 13$ and $\lambda_z^+ = 120$ in the full spectrum, which is a clear reflection of the frequently quoted near-wall streaky structures of streamwise velocity in wall-bounded turbulent flows. For v'' , as shown in Fig. 24(b), an energy peak with $\lambda_z^+ = 83$ emerges in the buffer layer $y^+ = 37$, which is likely associated with the short and tall vortical structures, as suggested by Cheng *et al.*³⁵ For T'' , the spectra in Fig. 24(c) exhibit a pattern similar to u'' , with clear evidence for small-scale organizations related to the thermal streaks with $\lambda_z^+ = 160$ at $y^+ = 27$. It is confirmed that the first mode is indeed exhibited by the small-scale structures of velocity and temperature in the near-wall region.

Regarding the other three modes, the spectra of u'' , v'' , and T'' shown in Figs. 25–27 highlight two important observations. First, as the mode number is increased, the wall-normal location of the energy peak moves away from the wall, with the characteristic spanwise wavelength gradually becoming larger. For the second and third modes, all the spectra peak in the overlap region within $y^+ < 100$, except for the spectra of v'' in Fig. 26(b), centering at $y^+ = 115$. The second modes in Fig. 25 share similar length scales $\lambda_z^+ \approx 166$ –182, which is a signature of the near-wall quasi-streamwise vortices observed by Kim *et al.*⁶⁶ and Jeong *et al.*⁶⁷ In Fig. 26, it can be seen that the third mode is characterized by a larger spanwise wavelength $\lambda_z^+ \approx 327$ –387 or $\lambda_z \approx 0.4\delta$ – 0.5δ . Such a value has previously been found by Fan *et al.*,³³ who argued that it corresponded to the energy-containing motions associated with self-similar Townsend eddies. Figure 27 highlights that

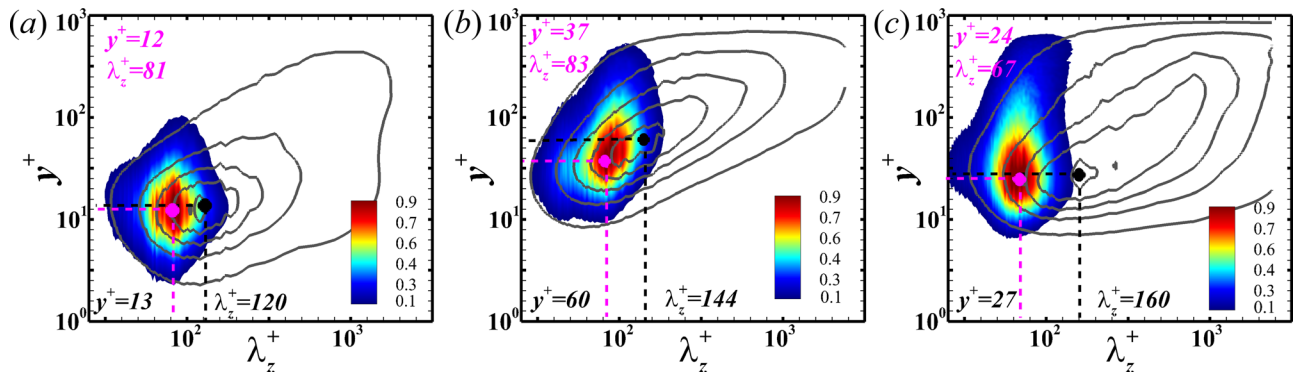


FIG. 24. Premultiplied spanwise spectra of the decomposed fluctuations in the first mode: (a) streamwise velocity; (b) wall-normal velocity; (c) temperature. The spectra are normalized by the respective maximum values. The black and pink solid circles denote the peak locations of the spectra for the raw DNS and the first mode, respectively. The full spectra are denoted by five equally spaced isolines from 0.1 to 0.9, which are marked with black solid lines from outward to inward.

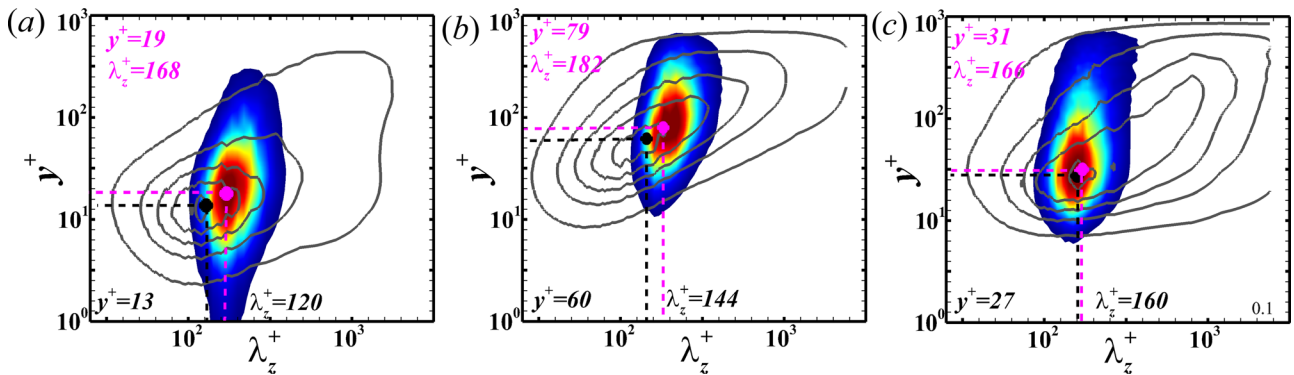


FIG. 25. Premultiplied spanwise spectra of the decomposed fluctuations in the second mode: (a) streamwise velocity; (b) wall-normal velocity; (c) temperature. See Fig. 24 for the legend.

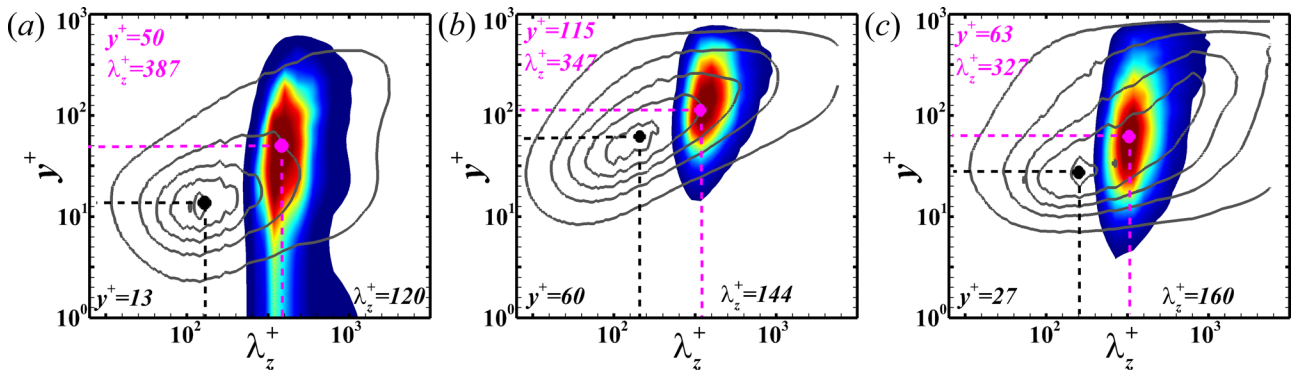


FIG. 26. Premultiplied spanwise spectra of the decomposed fluctuations in the third mode: (a) streamwise velocity; (b) wall-normal velocity; (c) temperature. See Fig. 24 for the legend.

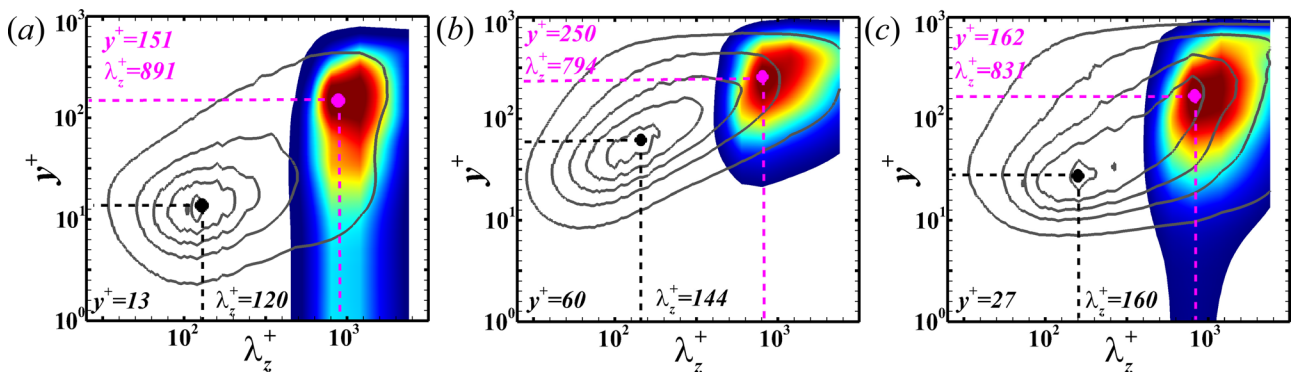


FIG. 27. Premultiplied spanwise spectra of the decomposed fluctuations in the fourth mode: (a) streamwise velocity; (b) wall-normal velocity; (c) temperature. See Fig. 24 for the legend.

all the spectra are centered in the large- (y^+, λ_z^+) domain, attaining an outer peak at $y^+ \approx 151\text{--}250$ and $\lambda_z \approx 0.9\delta\text{--}1.2\delta$, indicating that the fourth modes can be attributed to the large-scale motions and very-large-scale motions of superstructures located in the logarithmic region, such as those found by Hwang⁶⁸ and Hutchins and Marusic.⁶⁹ Based on the analysis above, the original velocity and temperature

fluctuations are synthesized by four different groups of structure with increasing characteristic spanwise wavelengths from the near-wall region to the outer region.

Second, the figures also support the wall-attached character of the outer large-scale streamwise velocity structure, whose footprint in the near-wall region is visible in the form of the spectra of u'' and is

attached to the wall at low-wavenumber energy, which is a remarkable feature of Figs. 26(a) and 27(a). As can be seen in Fig. 27(c), a quantitatively similar pattern is observed in the spectra of large-scale T'' , except that the imprint on the inner region become slighter weaker compared with u'' . These results are in accordance with the autocorrelation analysis of supersonic TBLs conducted by Pirozzoli and Bernardini,² who reported that the outer streamwise velocity and temperature structures were attached to the wall, but the influence of T -bearing eddies on the near-wall region was less apparent than that of the u -bearing eddies. In addition, it is found that the spectra of large-scale v'' reported are clearly detached from the wall, and no evident imprint on the inner region is observed.

To assess the contribution of velocity and temperature structures with characteristic spanwise length scales to the generation of the Reynolds shear stress and wall-normal heat flux, comparisons of the 16 decomposed components in Eqs. (13) and (14) with the raw DNS data are plotted vs y^+ in Fig. 28. The present results highlight an extremely precise collapse of the sum of the 16 components onto the full profiles of the Reynolds shear stress and wall-normal heat flux throughout the boundary layer, further confirming the excellent accuracy of the BEMD method. For $-u''v''$ and $-v''T''$, we observe that

the four diagonal terms in Figs. 28(a) and 28(c) are clearly dominant over the other 12 nondiagonal terms in Figs. 28(b) and 28(d). The predominance of the component (1, 1) in $-u''v''$ is a good indicator of the important role played by the small-scale structures of u'' and v'' in the near-wall region (see Fig. 24). A particularly striking feature in $-v''T''$ is the more prominent role of the component (4, 4), which characterizes the large-scale structures of v'' and T'' in the outer region (see Fig. 27). Thus, it is reasonable to infer that the full Reynolds shear stress is mostly related to the near-wall small-scale structures, whereas the full wall-normal heat flux is mainly dominated by the outer large-scale structures.

The decomposition of the $C_{f,T}$ contribution obtained by integrating the 16 components of $-u''v''$ over the boundary layer is shown in Fig. 29(a). As expected, the four diagonal terms contribute approximately 72% of $C_{f,T}$, with the small-scale component (1,1) being dominant, accounting for about 34.44% of the $C_{f,T}$ generation. For $C_{h,RS}$, a similar pattern is also identified in Fig. 29(b). Obviously, most of $C_{h,RS}$ comes from the four diagonal components, attaining up to about 69%, with the small-scale component (1,1) still taking the leading role, contributing about 27.52% of the work of the Reynolds stresses. Given the significant positive contributions of $C_{f,T}$ and $C_{h,RS}$ to the generation of

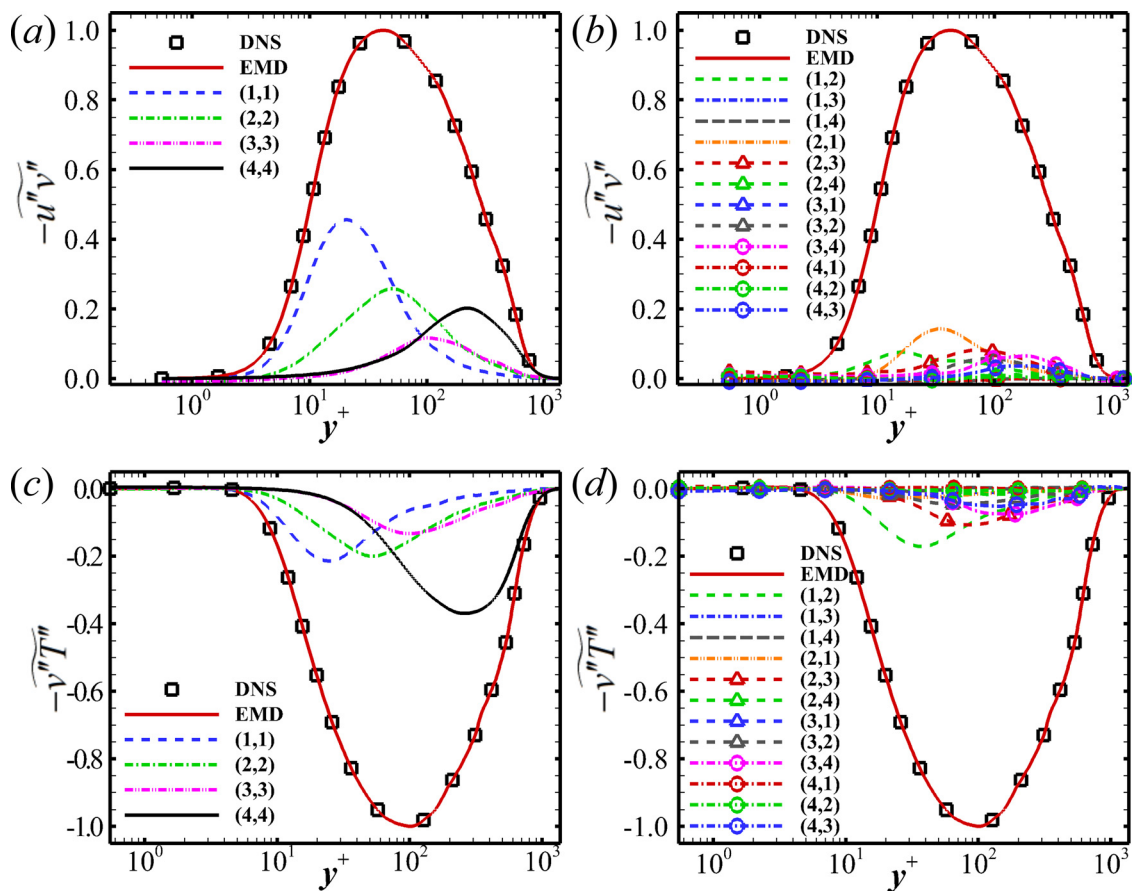


FIG. 28. Profiles of (a) and (b) the decomposed Reynolds shear stress and (c) and (d) the decomposed vertical heat flux: (a) and (c) the four diagonal terms; (b) and (d) the 12 nondiagonal terms. The profiles are normalized by the maximum value of the raw DNS.

Downloaded from http://pubs.aip.org/aip/pof/article-pdf/doi/10.1063/5.0079230/16624619/1015127_1_online.pdf

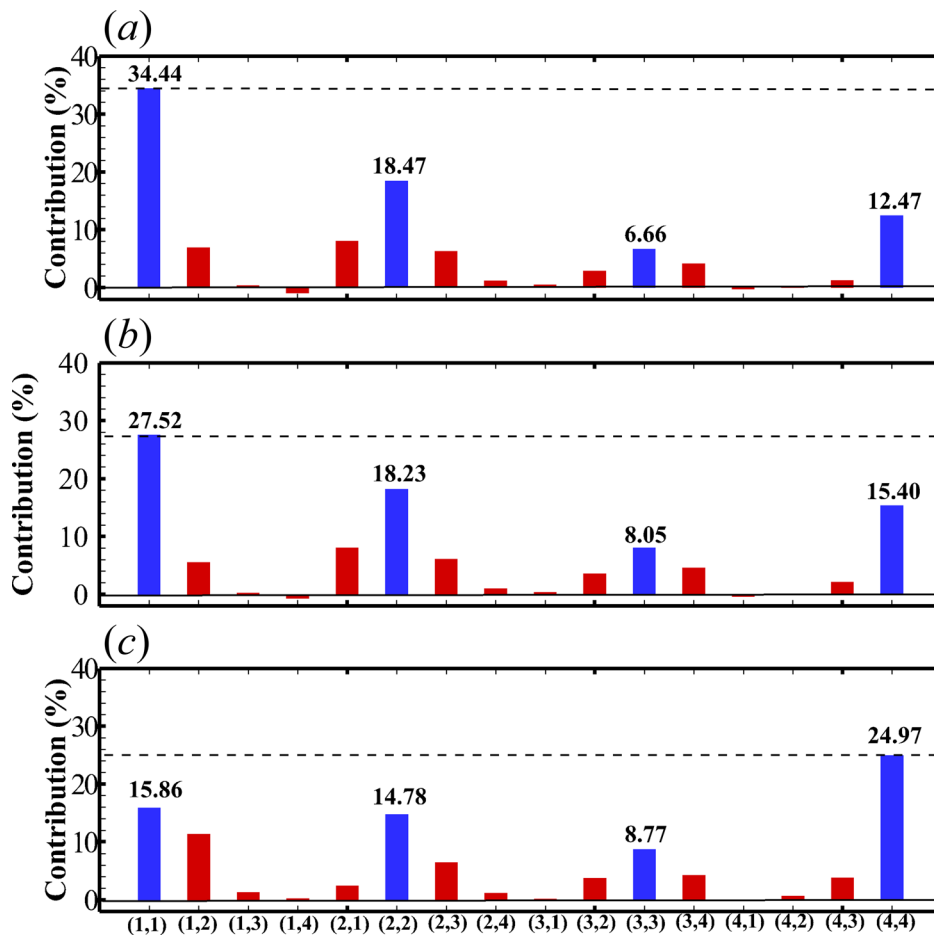


FIG. 29. Decomposition of the most significant contribution: (a) $C_{f, \bar{t}}$; (b) $C_{h,RS}$; (c) $C_{h,TH}$. The diagonal and nondiagonal components are denoted by blue and red bars, respectively.

C_f and C_h , respectively, the above results quantitatively support the conjecture that the generation of mean skin friction and heat transfer at the wall is most likely linked to the small-scale energy-containing structures residing in the near-wall region. Similarly, we perform a decomposition of $C_{h,TH}$ by integrating the 16 components of $-v''T''$ over the boundary layer, as shown in Fig. 29(c). The sum of the four diagonal components reaches approximately 64% of $C_{h,TH}$, and it should be stressed that the predominance of the small-scale component (1, 1) is overtaken by the large-scale component (4, 4), which is about 24.97%. This implies that the large-scale structures located in the logarithmic and outer regions make the greatest contribution to the upward transport of excessive heat at the wall in the present study.

IV. CONCLUSIONS

The characteristics of wall shear stress (WSS) and wall heat flux (WHF) have been numerically investigated using a database from DNS of a supersonic turbulent boundary layer at $M_\infty = 2.25$ and $Re_\tau = 769$. The analysis has shown that the rms of the WSS collapses well onto the correlation proposed by Abe *et al.*,⁸ while the rms of the WHF is found to follow a similar logarithmic dependence on Re_τ but with a larger constant of 0.457. A PDF analysis suggests that the WSS is characterized by a lognormal distribution, while the PDF tails of the

WHF become much wider. Compared with the WSS signal, the fluctuating WHF exhibits a significantly higher dominant frequency, a decreased streamwise extent, and an increased spanwise extent. A space-time correlation map reveals that the fluctuating WHF propagates downstream faster than the fluctuating WSS at $0.55U_\infty$ to $0.62U_\infty$ for q' and at $0.42U_\infty$ to $0.49U_\infty$ for τ' .

The conditionally averaged flow field confirms that extreme positive (EP) WSS and WHF fluctuation events are detected below a strong Q4 event. The EP event of τ' is clearly related to the downwash motion induced by a pair of strong quasi-streamwise vortices, which transports high-speed fluid from the outer region toward the wall. By contrast, the EP event of q' is the result of downward extrusion of low-temperature flow onto the high-temperature flow covering the wall. A conditional analysis of EN events reveals a completely different scenario, supporting the essential role of a pair of attached oblique vortices extending downstream. The EN event of τ' is associated with a low-speed streak, which is significantly compressed by the top-down motions of the outer high-speed flow. It is revealed that the EN event of q' is generated by direct impingement of the low-temperature flow originating from the outer region, which penetrates the high-temperature flow with a large wall-normal velocity and finally reaches the wall.

A decomposition analysis shows that the two contributing terms, direct viscous dissipation C_{fV} and turbulence kinetic energy production C_{fT} , yield approximately 90% of the mean wall skin friction, whereas the mean wall heat transfer is dominated mainly by a very large positive term C_{hRS} related to the work of the Reynolds stresses, which counteracts a large negative contribution C_{hTH} associated with turbulent transport of heat. With the help of the BEMD method, the velocity and temperature fluctuations have been decomposed into four modes according to the spanwise length scale. The integral of the decomposed Reynolds shear stress and wall-normal heat flux over the boundary layer suggests that the near-wall small-scale structures make a significant contribution to C_{fT} and C_{hRS} , whereas the large-scale structures in the logarithmic and outer regions contribute mainly to C_{hTH} , playing a leading role in transporting excess heat away from the wall.

ACKNOWLEDGMENTS

This study was supported by the National Natural Science Foundation of China (Nos. 11972356, 92052301, 2072306, and 91852203) and the National Key R&D Program of China (No. 2019YFA0405300).

AUTHOR DECLARATIONS

Conflict of Interest

The authors have no conflicts to disclose.

DATA AVAILABILITY

Some or all data, models, or code generated or used during the study are available from the corresponding author by request.

REFERENCES

- E. F. Spina, "The physics of supersonic turbulent boundary layers," *Annu. Rev. Fluid Mech.* **26**, 287–319 (1994).
- S. Pirozzoli and M. Bernardini, "Turbulence in supersonic boundary layers at moderate Reynolds number," *J. Fluid Mech.* **688**, 120–168 (2011).
- M. J. Ringuelet, M. Wu, and M. P. Martin, "Coherent structures in direct numerical simulation of turbulent boundary layer at Mach 3," *J. Fluid Mech.* **594**, 59–69 (2008).
- S. Pirozzoli, M. Bernardini, and F. Grasso, "Characterization of coherent vertical structures in a supersonic turbulent boundary layer," *J. Fluid Mech.* **613**, 205–231 (2011).
- M.-B. Sun, N. D. Sandham, and Z.-W. Hu, "Turbulence structures and statistics of a supersonic turbulent boundary layer subjected to concave surface curvature," *J. Fluid Mech.* **865**, 60–99 (2019).
- Q.-C. Wang, Z.-G. Wang, M.-B. Sun, R. Yang, Y.-X. Zhao, and Z.-W. Hu, "The amplification of large-scale motion in a supersonic concave turbulent boundary layer and its impact on the mean and statistical properties," *J. Fluid Mech.* **863**, 454–493 (2019).
- M. Fischer, J. Jovanovic, and F. Durst, "Reynolds number effects in the near-wall region of turbulent channel flow," *Phys. Fluids* **13**, 1755–1767 (2001).
- H. Abe, H. Kawamura, and H. Choi, "Very large-scale structures and their effects on the wall shear-stress fluctuations in a turbulent channel flow up to $Re_\tau = 640$," *J. Fluids Eng.* **126**, 835–843 (2004).
- Z.-W. Hu, C. L. Morfey, and N. D. Sandham, "Wall pressure and shear stress spectra from direct numerical simulations of channel flow up to $Re_\tau = 1440$," *AIAA J.* **44**, 1541–1549 (2006).
- R. Örlü and P. Schlatter, "On the fluctuating wall-shear stress in zero pressure-gradient turbulent boundary layer flows," *Phys. Fluids* **23**, 021704 (2011).
- C. D. Daniel, S. Laizet, and J. C. Vassilico, "Wall shear stress fluctuations: Mixed scaling and their effects on velocity fluctuations in a turbulent boundary layer," *Phys. Fluids* **29**, 055102 (2017).
- A. Wietrzak and R. M. Lueptow, "Wall shear stress and velocity in a turbulent axisymmetric boundary layer," *J. Fluid Mech.* **259**, 191–218 (1994).
- S. Jeon, H. Choi, J. Y. Yoo, and P. Moin, "Space-time characteristics of the wall shear-stress fluctuations in a low-Reynolds-number channel flow," *Phys. Fluids* **11**, 3084 (1999).
- S. Grosse and W. Schröder, "Wall-shear stress patterns of coherent structures in turbulent duct flow," *J. Fluid Mech.* **633**, 147–158 (2009).
- C. Brücker, "Signature of varicose wave packets in the viscous sublayer," *Phys. Fluids* **20**, 061701 (2008).
- B. Nottebrock, K. J. Genurts, and W. Schröder, "Wall-shear stress measurements in an adverse pressure gradient turbulent boundary layer," AIAA Paper No. 2014-2098, 2014.
- F.-L. Tong, J.-Q. Chen, D. Sun, and X.-L. Li, "Wall-shear stress fluctuations in a supersonic turbulent boundary layer over an expansion corner," *J. Turbul.* **21**, 355–374 (2020).
- J. Sheng, E. Malkiel, and J. Katz, "Buffer layer structures associated with extreme wall stress events in a smooth wall turbulent boundary layer," *J. Fluid Mech.* **633**, 17–60 (2009).
- C. Pan and Y. Kwon, "Extremely high wall-shear stress events in a turbulent boundary layer," *J. Phys.: Conf. Ser.* **1001**, 012004 (2018).
- N. Hutchins, J. P. Monty, B. Ganapathisubramani, H. C. H. Ng, and I. Marusic, "Three-dimensional conditional structure of a high-Reynolds-number turbulent boundary layer," *J. Fluid Mech.* **673**, 255–285 (2011).
- G. Gomit, R. de Kat, and B. Ganapathisubramani, "Structure of high and low shear-stress events in a turbulent boundary layer," *Phys. Rev. Fluids* **3**, 014609 (2018).
- B. Guerrero, M. F. Lamber, and R. C. Chin, "Extreme wall shear stress events in turbulent pipe flows: Spatial characteristics of coherent motions," *J. Fluid Mech.* **904**, A18 (2020).
- K. Fukagata, K. Iwamoto, and N. Kasagi, "Contribution of Reynolds stress distribution to the skin friction in wall-bounded flows," *Phys. Fluids* **14**, L73–L76 (2002).
- Y. Peet and P. Sagaut, "Theoretical prediction of turbulent skin friction on geometrically complex surfaces," *Phys. Fluids* **21**, 105105 (2009).
- A. Bannier, E. Garnier, and P. Sagaut, "Riblet flow model based on an extended FIK identity," *Flow Turbul. Combust.* **95**, 351–376 (2009).
- D. Modesti, S. Pirozzoli, P. Orlandi, and F. Grasso, "On the role of secondary motions in turbulent square duct flow," *J. Fluid Mech.* **847**, R1 (2018).
- Y. Kametani, K. Fukagata, R. Örlü, and P. Schlatter, "Effect of uniform blowing/suction in a turbulent boundary layer at moderate Reynolds number," *Int. J. Heat Fluid Flow* **55**, 132–142 (2015).
- N. Renard and S. Deck, "A theoretical decomposition of mean skin friction generation into physical phenomena across the boundary layer," *J. Fluid Mech.* **790**, 339–367 (2016).
- W.-P. Li, Y.-T. Fan, D. Modesti, and C. Cheng, "Decomposition of the mean skin-friction drag in compressible turbulent channel flows," *J. Fluid Mech.* **875**, 101–123 (2019).
- Y.-T. Fan, W.-P. Li, and S. Pirozzoli, "Decomposition of the mean skin-friction drag in zero-pressure-gradient turbulent boundary layers," *Phys. Fluids* **31**, 086105 (2019).
- F.-L. Tong, J.-Y. Duan, and X.-L. Li, "Characteristics of reattached boundary layer in shock wave and turbulent boundary layer interaction," *Chin. J. Aeronaut.* (in press) (2022).
- Z. G. Zhang, F.-L. Tong, J.-Y. Duan, and X.-L. Li, "Direct numerical simulation of supersonic turbulent expansion corner with shock impingement," *Phys. Fluids* **33**, 105104 (2021).
- Y.-T. Fan, W.-P. Li, M. Atzori, R. Pozuelo, P. Schlatter, and R. Vinuesa, "Decomposition of the mean skin-friction drag in adverse-pressure-gradient turbulent boundary layers," *Phys. Rev. Fluids* **5**, 114608 (2020).
- D. Sun, Q.-L. Guo, X.-X. Yuan, H.-Y. Zhang, and C. Li, "A decomposition formula for the wall heat flux of a compressible boundary layer," *Adv. Aerodyn.* **3**, 33 (2021).
- C. Cheng, W.-P. Li, A. Lozano-Durán, and H. Liu, "Identity of attached eddies in turbulent channel flows with bidimensional empirical mode decomposition," *J. Fluid Mech.* **870**, 1037–1071 (2019).
- F.-L. Tong, X.-L. Li, Y.-H. Duan, and C.-P. Yu, "Direct numerical simulation of supersonic turbulent boundary layer subjected to a curved compression ramp," *Phys. Fluids* **29**, 125101 (2017).

- ³⁷F.-L. Tong, C.-P. Yu, Z.-G. Tang, and X.-L. Li, "Numerical studies of shock wave interactions with a supersonic turbulent boundary layer in compression corner: Turning angle effects," *Comput. Fluids* **149**, 56–69 (2017).
- ³⁸X.-K. Zhu, C.-P. Yu, F.-L. Tong, and X.-L. Li, "Numerical study on wall temperature effects on shock wave/turbulent boundary layer interaction," *AIAA J.* **55**, 131–140 (2017).
- ³⁹F.-L. Tong, D. Sun, and X.-L. Li, "Direct numerical simulation of impinging shock wave and turbulent boundary layer interaction over a wavy-wall," *Chin. J. Aeronaut.* **34**, 350–363 (2021).
- ⁴⁰H. Gao, D.-X. Fu, Y.-W. Ma, and X.-L. Li, "Direct numerical simulation of supersonic turbulent boundary layer," *Chin. Phys. Lett.* **22**, 1709–1712 (2005).
- ⁴¹M. P. Martin, E. M. Taylor, M. Wu, and V. G. Weirs, "A bandwidth-optimized WENO scheme for the effective direction numerical simulation of compressible turbulence," *J. Comput. Phys.* **220**, 270–289 (2006).
- ⁴²M. Wu and M. P. Martin, "Direct numerical simulation of supersonic turbulent boundary layer over a compression ramp," *AIAA J.* **45**, 879–889 (2007).
- ⁴³G. Jiang and C. Shu, "Efficient implementation of weighted ENO schemes," *J. Comput. Phys.* **126**, 202–228 (1996).
- ⁴⁴S. Gottlieb and C. W. Shu, "Total variation diminishing Runge–Kutta schemes," *Math. Comput.* **67**, 73–85 (1998).
- ⁴⁵S. Pirozzoli, F. Grasso, and T. B. Gatski, "Direct numerical simulation and analysis of a spatially evolving supersonic turbulent boundary layer at $M = 2.25$," *Phys. Fluids* **16**, 530 (2004).
- ⁴⁶J. Fang, A. A. Zheltovodov, Y.-F. Yao, C. Moulinec, and D. R. Emerson, "On the turbulence amplification in shock-wave/turbulent boundary layer interaction," *J. Fluid Mech.* **897**, A32 (2020).
- ⁴⁷M. Bernardini and S. Pirozzoli, "Wall pressure fluctuations beneath supersonic turbulent boundary layers," *Phys. Fluids* **23**, 085102 (2011).
- ⁴⁸X.-S. Wu, J.-H. Liang, and Y.-X. Zhao, "Direct numerical simulation of a supersonic turbulent boundary layer subjected to a concave surface," *Phys. Rev. Fluids* **4**, 044602 (2019).
- ⁴⁹M. V. Morkovin, "Effects of compressibility on turbulent flows," in *Mécanique de la turbulence*, edited by A. Favre (CNRS, Paris, 1961), pp. 367–380.
- ⁵⁰P. Schlatter and R. Örlü, "Assessment of direct numerical simulation data of turbulent boundary layers," *J. Fluid Mech.* **659**, 116–126 (2010).
- ⁵¹S. Pirozzoli, M. Bernardini, and F. Grasso, "Direct numerical simulation of transonic shock/boundary layer interaction under conditions of incipient separation," *J. Fluid Mech.* **657**, 361–393 (2010).
- ⁵²S. P. Gravante, A. M. Naguib, C. E. Wark, and H. M. Nagib, "Characterization of the pressure fluctuations under a fully developed turbulent boundary layer," *AIAA J.* **36**, 1808–1816 (1998).
- ⁵³T. Farabee and M. J. Casarella, "Spectral features of wall pressure fluctuations beneath turbulent boundary layers," *Phys. Fluids* **3**, 2410–2420 (1991).
- ⁵⁴J. Jimenez, S. Hoyas, M. P. Simens, and Y. Mizuno, "Turbulent boundary layers and channels at moderate Reynolds numbers," *J. Fluid Mech.* **657**, 335–360 (2010).
- ⁵⁵P. Schlatter and R. Örlü, "Turbulent boundary layers at moderate Reynolds numbers: Inflow length and tripping effects," *J. Fluid Mech.* **710**, 5–34 (2012).
- ⁵⁶K. R. Sreenivasan and R. A. Antonia, "Properties of wall shear stress fluctuations in a turbulent duct flow," *Trans. ASME: J. Appl. Mech.* **44**, 389–395 (1977).
- ⁵⁷G. I. Park and P. Moin, "Space–time characteristics of wall-pressure and wall shear-stress fluctuations in wall-modeled large eddy simulation," *Phys. Rev. Fluids* **1**, 024404 (2016).
- ⁵⁸L. Duan, M. M. Choudhari, and C. Zhang, "Pressure fluctuations induced by a hypersonic turbulent boundary layer," *J. Fluid Mech.* **804**, 578–607 (2016).
- ⁵⁹C. Chin, R. Vinuesa, R. Örlü, J. I. Cardesa, A. Noorani, P. Schlatter, and M. S. Chong, "Flow topology of rare back flow events and critical points in turbulent channels and toroidal pipes," *J. Phys.: Conf. Ser.* **1001**, 012002 (2018).
- ⁶⁰P. Lenaers, Q. Li, G. Brethouwer, P. Schlatter, and R. Örlü, "Rare backflow and extreme wall-normal velocity fluctuations in near-wall turbulence," *Phys. Fluids* **24**, 035110 (2012).
- ⁶¹J. H. Lee and H. J. Sung, "Very-large-scale motions in a turbulent boundary layer," *J. Fluid Mech.* **673**, 80–120 (2011).
- ⁶²R. J. Adrian, C. D. Meinhart, and C. D. Tomkins, "Vortex organization in the outer region of the turbulent boundary layer," *J. Fluid Mech.* **422**, 1–54 (2000).
- ⁶³J. I. Cardesa, J. P. Monty, J. Soria, and M. S. Chong, "The structure and dynamics of backflow in turbulent channels," *J. Fluid Mech.* **880**, R3 (2019).
- ⁶⁴M. Bross, T. Fuchs, and C. Kähler, "Interaction of coherent flow structures in adverse pressure gradient turbulent boundary layers," *J. Fluid Mech.* **873**, 287–321 (2019).
- ⁶⁵L. Agostini, M. Leschziner, J. Poggie, N. J. Bisek, and D. V. Gaitonde, "Multi-scale interactions in a compressible boundary layer," *J. Turbul.* **18**, 760–780 (2017).
- ⁶⁶J. Kim, P. Moin, and R. Moser, "Turbulence statistics in fully developed channel flow at low Reynolds number," *J. Fluid Mech.* **177**, 133–166 (1987).
- ⁶⁷J. Jeong, F. Hussain, W. Schoppa, and J. Kim, "Coherent structures near the wall in a turbulent channel flow," *J. Fluid Mech.* **332**, 185–214 (1997).
- ⁶⁸Y. Hwang, "Statistical structure of self-sustaining attached eddies in turbulent channel flow," *J. Fluid Mech.* **767**, 254–289 (2015).
- ⁶⁹N. Hutchins and I. Marusic, "Evidence of very long meandering features in the logarithmic region of turbulent boundary layers," *J. Fluid Mech.* **579**, 1–28 (2007).